RESEARCH ARTICLE

Editor's Choice

ADVANCED MATERIALS INTERFACES Open Access

www.advmatinterfaces.de

Understanding the Influence of Serum Proteins Adsorption on the Mechano-Bactericidal Efficacy and Immunomodulation of Nanostructured Titanium

Karolinne Martins de Sousa, Denver P. Linklater, Vladimir A. Baulin,* Chaitali Dekiwadia, Edwin Mayes, Billy J. Murdoch, Phuc H. Le, Christopher J. Fluke, Veselin Boshkovikj, Cuie Wen, Russell J. Crawford, and Elena P. Ivanova**

Nanostructured surfaces are effective at physically killing bacterial cells, highlighting their prospective application as biomaterials. The benefits of application of mechano-bactericidal nanostructures as an alternative to chemical functionalisation are well documented, however, the effects of protein adsorption are not well understood. In this work, theoretical and experimental analyses are conducted by studying the adsorption of human serum proteins (HSP) to nanosheet titanium (Ti) and its subsequent effect on the mechano-bactericidal efficacy toward *Staphylococcus aureus* and *Pseudomonas aeruginosa* cells. The nanosheet pattern exhibits enhanced antibiofouling behaviour mantaining high bactericidal efficiency toward both Gram-negative and Gram-positive cells in the presence of adsorbed HSP. To ascertain the immunomodulatory response, *S. aureus* cells are introduced to protein-conditioned Ti nanosheet surfaces prior to introducing RAW 264.7 macrophages. On the pre-infected nanostructured surfaces, macrophages exhibit wound healing behaviour with superior activation of M2-like macrophage polarization and secretion of anti-inflammatory cytokines. By contrast, macrophages attached to infected smooth surfaces activated the M1-like polarized phenotype via the high expression of pro-inflammatory cytokines, indicating persistent inflammation. The outcomes of this work demonstrate the suitability of Ti nanosheets as a potential biomaterial surface whereby the mechano-bactericidal activity is not compromised by HSP adsorption and, furthermore, positively influenced an anti-inflammatory immune response.

1. Introduction

Ti implantable biomaterials are widely used in orthopedics and dentistry for the treatment of large bone defects, fixation of fractures, and to address musculoskeletal disorders.[1] Implantable devices predominantly interact with host bone tissues at their interface, exerting an important influence on protein adsorption and the subsequent migration of host cells.[2] As such, specific control of the host cell-material interactions is beneficial to improving implant performance.[3] The surface of implantable devices can be modified to increase implant-cell interactions to ensure a long-term and stable fixation.

All devices surgically implanted within the host body generate an inflammatory response due to the inevitable wound injury that accompanies device implantation.[4] The direct contact of the implanted device with host blood will cause serum proteins to rapidly adsorb onto the biomaterial interface.[5] The provisional protein layer becomes a matrix

K. Martins de Sousa, D. P. Linklater, P. H. Le, R. J. Crawford, E. P. Ivanova
School of Science, STEM College
RMIT University
Melbourne, Victoria 3000, Australia
E-mail: denver.linklater@unimelb.edu.au; elena.ivanova@rmit.edu.au

The ORCID identification number(s) for the author(s) of this article can be found under https://doi.org/10.1002/admi.202301021

[+]Present address: Helix Animation, St Clement of Ohrid 31, Bitola 7000, North Macedonia

DOI: 10.1002/admi.202301021

D. P. Linklater
Department of Biomedical Engineering, Graeme Clark Institute
The University of Melbourne
Parkville, Victoria 3010, Australia

V. A. Baulin
Departament d'Enginyeria Quimica
Universitat Rovira i Virgili
Tarragona 43007, Spain
E-mail: S3777891@student.rmit.edu.au

C. Dekiwadia, E. Mayes, B. J. Murdoch
RMIT Microscopy and Microanalysis Facility, STEM College
RMIT University
Melbourne, Victoria 3000, Australia

C. J. Fluke, V. Boshkovikj[+]
Swinburne University of Technology
Hawthorn, Victoria 3122, Australia

C. Wen
School of Engineering, STEM College
RMIT University
Melbourne, Victoria 3000, Australia

by which to recruit immune cells and initiate the foreign body response (FBR). The inflammatory FBR begins as an acute inflammatory phase whereby monocytes and macrophages are attracted to the implanted device and mediate an attack as well as secreting further inflammatory markers. Over time, macrophages colonise the implant surface and aid in the transition from acute FBR to the chronic phase of FBR. Previous studies have determined that the surface roughness and topography of Ti biomaterials mediate macrophage adhesion and the secretion of proinflammatory markers.[6]

Biomaterial nanoscale roughness exerts a stronger immunomodulatory response than implant surfaces with microscale roughness.[7] In addition, macrophages are sensitive to the specific nanoscale architecture of implant surfaces and can influence the tissue–implant interactions via M1/M2 polarization. For example, research on anodised Ti implant surfaces possessing Ti nanotubes (NTs) has shown that NTs with diameters of 30 nm induced the M2 polarization of human macrophages in vitro, and, consequently, a reduced inflammatory response when compared to NTs surfaces with larger diameters (80 nm).[7,8] The NTs with larger diameters elicited a pro-inflammatory M1 polarization response. It was also reported that Ti nanowire surfaces produced via a hydrothermal etching treatment modulated protein adsorption and induced the anti-inflammatory M2 polarization of adhered macrophages.[9]

Despite intensive efforts toward improvement of tissue regeneration while interacting with biomaterial surfaces, implant-related bacterial infections frequently occur and are responsible for ≈ 45% of all nosocomial infections.[10] Implant-related infections are often resistant to standard antibiotic treatment and persist until the implant is removed, leading to life-threatening complications for the patient.[11] Previously, our group demonstrated the role of surface nanoscale topography toward imparting mechanical bactericidal activity to implant surfaces.[12] Mechano-bactericidal nanostructured surfaces can eliminate pathogenic bacteria through the physical rupture of adhering bacterial cells. Bacterial cell death through mechanical means is a promising substitute for chemical-based antibacterial biomaterial coatings.[13]

Hydrothermal treatment represents an efficient and facile nanofabrication approach to synthesizing nanostructures possessing high mechano-bactericidal properties.[12f,14] Using a hydrothermal etching method, we recently developed nanosheet-like Ti surfaces that inactivated 99% of *P. aeruginosa* and 90% of *S. aureus* bacterial cells.[12f] Furthermore, the Ti nanosheet pattern exhibited a remarkable modulation of osteogenic response combined with mechano-bactericidal activity [12f,14d,15] and promoted improved attachment, proliferation, and differentiation of eukaryotic cells.[15,16]

While surface topography play a major role in blood protein adsorption,[17] protein adsorption may also promote topographic and geometric alterations of nanofeatures (whose activity is primarily dependent on their topographical dimensions).[18] The interactions of total or whole serum proteins with complex nanostructured surfaces and their effects on the surface's bactericidal performance are not well-understood and require in-depth investigations.[19] Recent research has highlighted the importance of a protein adhesion layer modulating monocyte response to mechano-bactericidal hydrothermally etched Ti nanotopographies.[20] Given the pivotal role of an adsorbed protein layer in coordinating macrophage response, and in turn their role in determining the fate of implantation, it is important to fully characterise the immunomodulation of mechano-bactericidal nanostructured Ti surfaces. Therefore, in this study, the adsorption of HSP at different concentrations to hydrothermally treated Ti (HTTi) surfaces was characterized using a bicinchoninic acid (BCA) protein assay and high-resolution electron microscopy techniques. For theoretical analysis of the pattern of protein adsorption, a modified version of the Random Sequential Adsorption (RSA) model was employed. Furthermore, we aimed to evaluate the suitability of HTTi surfaces as an anti-infective biomaterial by design of an in vitro infection model. The infection model was designed to emulate a clinical case of implant-associated infection whereby the implant is contaminated with bacteria during, or directly after implantation. Thus, we considered the impact of adsorbed serum proteins on RAW 264.7 macrophage attachment, proliferation, phenotype, and inflammatory response.

2. Results

2.1. Surface Topography of HTTi

Hydrothermal etching is a simple, affordable, and template-free method of surface patterning Ti.[21] HTTi surfaces have been reported to exhibit high levels of bactericidal activity as well as increased cytocompatibility towards human cells.[14,22,23] In this work, we fabricated HTTi surfaces by exposing Ti discs to an alkaline hydrothermal treatment for 6 h at 150 °C.[12] The HTTi surface topographies were characterized using high-resolution scanning electron microscopy (SEM), as shown in **Figure 1A**. Examination of high magnification micrographs revealed the formation of a homogeneous and dense network of sheet-like nanostructures, with a nanoedge thickness of 10 ± 2 nm. The surface feature morphologies formed are due to the dissolution of Ti^{4+} from the oxide layer (TiO_2) and the subsequent surface precipitation of potassium titanate ($K_2Ti_3O_7$).[12,24] Over a 6 h reaction time, the dense network of blade-like nanosheets shown in the SEM images in Figure 1A is formed by an increased nucleation and growth rate over the longer reaction time, leading to a homogeneous coverage of interlocking nanosheets with sharp nanoedges. In contrast, the polished Ti (pTi) samples (used as a control surface) exhibited a conventional flat Ti topography. Surface roughness was evaluated using atomic force microscopy (AFM) (TableS1, Figure S1, Supporting Information). The fabrication of a nanotopography on the Ti surface led to enhanced levels of surface roughness, as shown in Table S1 (Supporting Information). The average surface roughness (S_a) significantly ($p < 0.001$) increased from 6.2 ± 3 nm (pTi) to 26.5 ± 4 nm (HTTi).

To evaluate the surface wettability of the Ti samples, a sessile drop water contact angles (WCA) were measured under ambient conditions. Prior to surface modification, the control pTi surface exhibited a WCA of 58.9 ± 6°, whereas after the hydrothermal treatment, the WCA decreased to 22 ± 2° (Figure 1A). These results indicated the increased hydrophilicity of the HTTi surfaces following etching.

Despite the marked change in surface hydrophilicity, the chemical composition of the surfaces was relatively unchanged

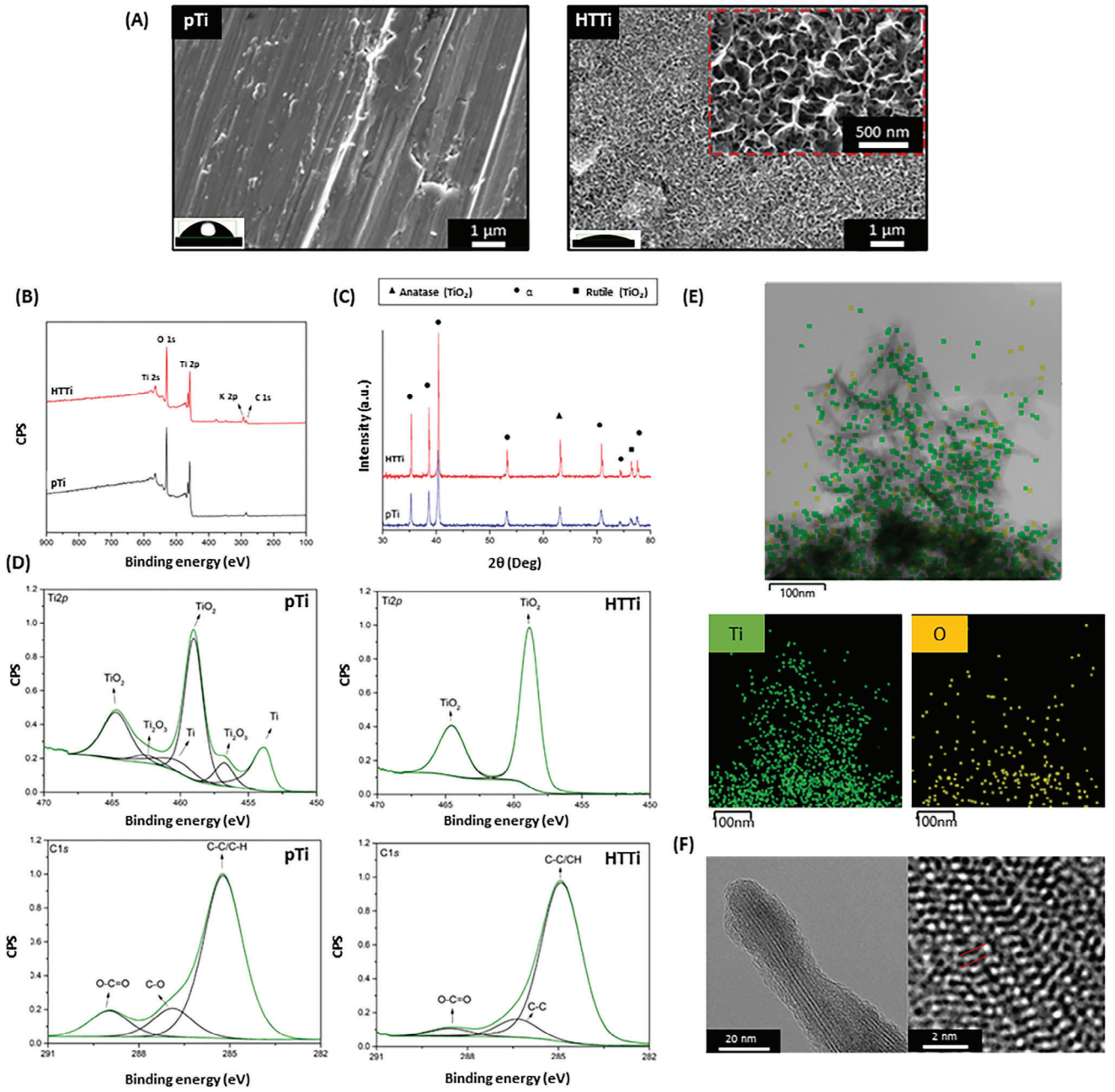

Figure 1. Surface characterization of pTi and nanotextured Ti surfaces. A) Representative SEM micrographs showing the topography of the Ti surfaces before and after hydrothermal treatment. Inset images show water contact angle (WCA) measurements. The HTTi surfaces exhibited a highly hydrophilic nature with a WCA of $22.0 \pm 2°$, whereas pTi surface exhibited a WCA of $58.9 \pm 6°$. B) XPS survey spectra of the different Ti surfaces. C) X-ray diffractograms showing the crystalline phases on the Ti surfaces: α-phase of Ti; anatase and rutile phases of TiO_2 phases. D) De-convoluted C 1*s* and Ti 2*p* XPS peak regions. E) STEM micrograph and corresponding EDS chemical maps of the HTTi nanosheets. F) HR-STEM dark-field micrograph of single TiO_2 nanosheet and lattice crystal structure.

after treatment. X-ray photoelectron spectroscopy (XPS) was performed to verify the chemical composition of the different Ti surfaces (Figure 1B and Figure 1D). The XPS survey spectra showed that the principal chemical components present on the Ti surfaces were Ti, carbon (C), and oxygen (O) (Figure 1B). The identification of K as a chemical component found only on HTTi surfaces was determined to be a consequence of the hydrothermal treatment, which led to the formation of potassium titanate ($K_2Ti_3O_7$). De-convoluted scans of the Ti 2*p* regions confirmed that the HTTi surfaces were mainly composed of TiO_2. The C 1*s* spectra indicated that the carbon present on the surface was attributed to C—C/C—H, C—O, and O—C═O bonds, which were found to be consistent with the ratios typically observed in "adventitious" carbon contamination. The analysis of O 1*s* peaks

re-confirmed the carbon contamination by revealing the presence of C═O and C—O. De-convoluted high-resolution XPS peaks are illustrated in Figure 1D.

X-ray diffraction (XRD) was performed to evaluate surface crystallinity. The diffractograms showed peaks that highlighted the crystallinity of the Ti surfaces (Figure 1C). High-intensity peaks at 35.3°, 38.6°, 40.3°, 53.2°, 70.8°, 74.3°, and 77.6° corresponded to the Ti a phase (JCPDS 44–1294).[15,25] The peaks at 63.1° and 76.4° indicated the presence of anatase and rutile phases, respectively (JCPDS No. 21–1272).[26] No substantial changes in the surface crystallinity between pTi and HTTi were detected. However, an enhanced formation of TiO_2 was observed for HTTi surfaces, with an increase in peak intensity being observed for both the anatase and α phases.

2.2. Protein Adsorption on HTTi Surfaces

The conditioning protein layer that rapidly forms on the surface after device placement is essential for the recruitment of immune cells, including macrophages.[27] Furthermore, the presence of serum proteins modulates host cell adhesions essential for the successful long-term implantation of medical devices.[28] To evaluate serum protein adsorption onto the nanotextured Ti surfaces, a BCA assay was used to comparatively analyse the amount of adsorbed HSP on non-structured (pTi) and HTTi surfaces as a function of protein concentration (**Figure 2A**). HSP adsorption was assessed at increasing concentrations of 0.1, 1, 10 and 100% following 1 h of incubation with the HTTi surfaces and the control, pTi. The amount of HSP adsorption was strongly concentration-dependent for both smooth and modified Ti surfaces; however, the total HSP adsorption was significantly increased on the nanotextured HTTi surfaces; in agreement with previously published observations that indicated that protein adsorption can be greater on nanostructured surfaces compared to smooth surfaces.[29] At higher serum concentrations, HSP adsorption was found to be 1.6 and 2.3 times greater ($p < 0.05$ at 10%; $p < 0.01$ at 100%, respectively) on HTTi surfaces than on their non-structured counterpart (pTi). An increase in initial protein concentration also results in an increased quantity of protein adsorbed.[30] Additionally, in the case of Ti, the inherent oxide layer present on the surface plays a significant role in influencing the adsorption of protein.[31]

Since albumin is the predominant protein detected in circulating HSP,[32] an in-depth assessment of the adsorption of albumin using bovine serum albumin (BSA) was also conducted. The structural similarity between BSA and human serum albumin frequently renders it as the preferred model for comparative studies.[33] Following BSA adsorption onto the different Ti surfaces (Figure 2B), the BCA assay indicated a similar adsorption pattern for BSA as previously determined for HSP. As well as more prominent in the HTTi surfaces than that in the pTi surfaces, quantification of adsorbed BSA determined to be a concentration-dependent process. At BSA concentrations of 10 and 100%, protein's adsorption was found to be 1.7 and 3 times greater ($p < 0.01$ at 10%; $p < 0.001$ at 100%, respectively) on the HTTi surfaces than on the control (pTi) surfaces.

These findings indicated that the roughness of HTTi surfaces has a notable impact on the adsorption of a single (BSA) or complex (HSP) serum proteins, as compared to the smooth pTi surfaces. Indeed, rough surfaces provide more surface area available for protein adsorption, leading to a greater amount of protein being adsorbed.[34] Additionally, pockets or crevices available on rougher surfaces act as physical traps for proteins, which also result in increased protein adsorption.[35] For example, Ti NTs was found to trap proteins, including collagen and bone morphogenetic protein 2 (BMP-2).[36] However, the increased protein adsorption may be also attributed to the increased hydrophilicity of HTTi surfaces. For example, hydrophobic surfaces are likely to increase overall protein adsorption, *e.g.*, immunoglobulin G2, which plays a role in the expression of pro-inflammatory cytokines by attached macrophages,[37,38] whereas hydrophilic surfaces have been shown to increase the adsorption of serum albumin.[39] The size of albumin facilitates protein diffusion through the stable layer of water molecules that forms on hydrophilic surfaces.[39] Moreover, albumin contains significant amounts of charged residues capable of forming unique contacts with hydrophilic surfaces, increasing the likelihood of its adsorption on such surfaces.[38,39]

The surface morphology of the HTTi nanosheets after HSP adsorption was investigated using SEM and scanning transmission electron microscopy (TEM/STEM). There was an evident increase in the nanosheet edge thickness (Figure 2C, D, and E), accompanied by the formation of protein aggregates on top and along the edge of the nanostructures resulting in an increase in edge thickness from 10 nm (surfaces with no HSP) to up to ≈ 21 nm (at HSP concentrations of 100%); however, interspace between the nanosheets remained free of proteins as clearly seen in **Figure 3D**. The increase in nanoedge thickness due to protein aggregation was correlated to an increase in protein concentration, as determined by the BCA assay. To further understand the adsorption of HSP on HTTi surfaces, high-resolution TEM/STEM was performed (Figure 2E). Analysis of TEM/STEM micrographs of the single nanosheets revealed that only a thin layer of ≈ 10 nm thin of amorphous material indicative of HSP (artificially coloured green), was built up around the nanosheet (seen as crystalline fringes and artificially coloured red).

2.3. Theoretical Analysis of Protein Adsorption on Nanotextured Ti Surfaces

In this study, we utilized a modified version of the RSA model to effectively analyze the localization of adsorbed human serum albumin on the nanotextured surfaces.[18] The blocking function, i.e., the probability to adsorb a protein at a surface, taking into account the presence of previously adsorbed proteins, is calculated as a function of the occupancy (Figure 3A). In turn, occupancy θ (Figure 3B) refers to the measurement or representation of how much space or surface area is covered or filled by adsorbed particles or molecules. The occupancy is a key parameter in understanding the extent to which the surface or substrate is covered by the adsorbed particles. Occupancy is expressed as a fraction, ranging from 0 to 1, where 0 represents an empty surface (no adsorption), and 1 represents a fully covered surface (complete adsorption). As particles are randomly and sequentially placed into an empty space without overlap, the occupancy increases, affecting the blocking function and the probability of finding an

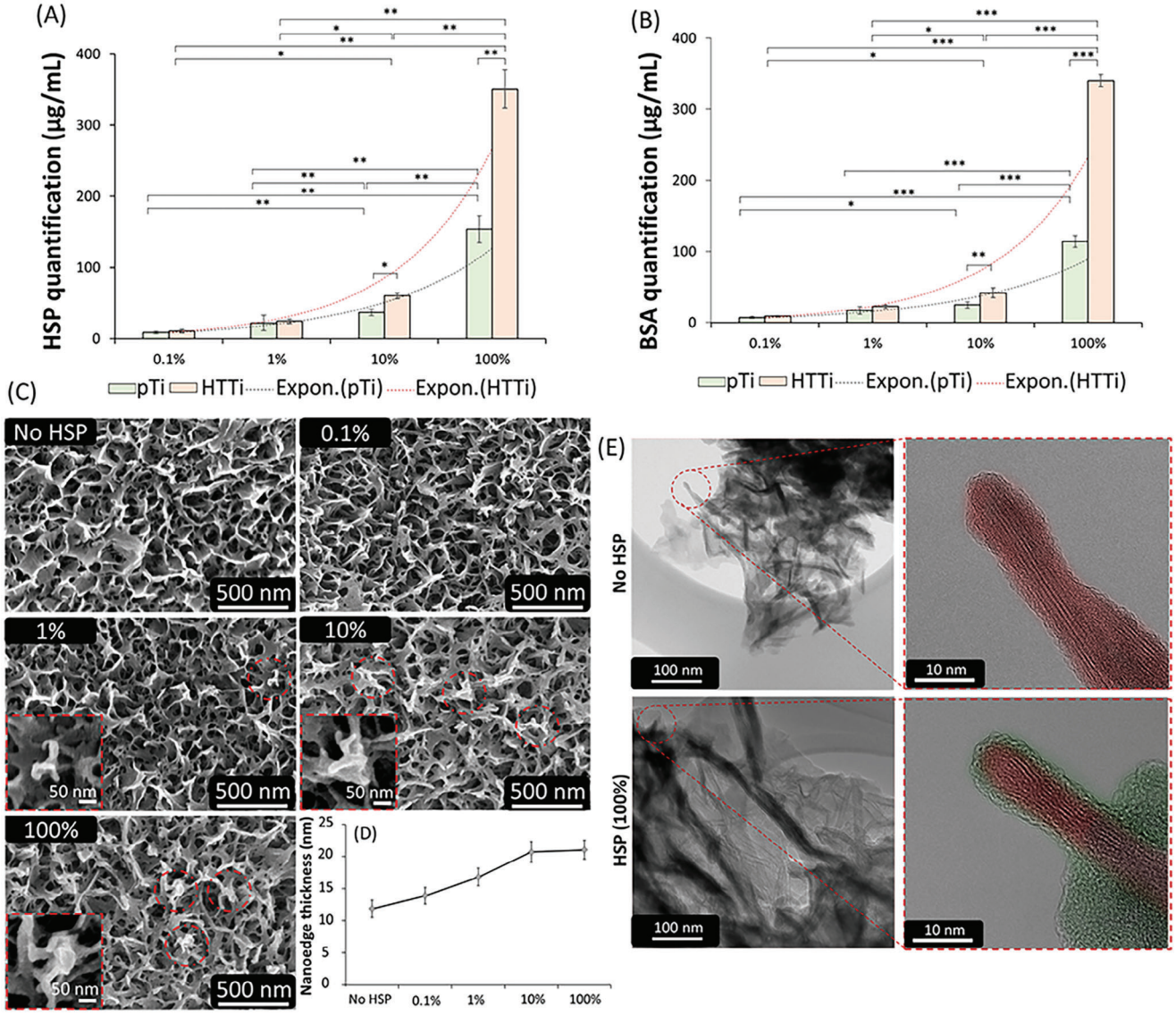

Figure 2. Protein adsorption on Ti surfaces. Quantification of A) HSP and B) BSA protein adsorption on pTi and HTTi surfaces using a BCA assay. The HTTi surfaces exhibited increased levels of protein adsorption compared to that observed on the smooth pTi surface. Statically significant differences are labelled as *($p < 0.05$); **($p < 0.01$); and ***($p < 0.001$). C) Representative SEM micrographs showing the topography of HTTi surfaces with adsorbed HSP at concentrations ranging from 0% (indicating no HSP) to 100%. At higher HSP concentrations, aggregates formed on top of the nanostructures (highlighted in red and detailed in the insets). The scale bars denote a length of 500 nm for the high-magnification SEM micrographs and 50 nm for the insets. D) Nanoedge thickness after HSP adsorption. An increase in nanosheet thickness was observed after increasing HSP concentrations. E) High-resolution TEM/STEM images of a single crystalline Ti nanosheet of ≈ 10 nm thin presented in vertical cross-section, (artificially coloured red). Following the adsorption of HSP at a concentration of 100%, an amorphous material, indicative of protein, was observed (artificially coloured in green) on the Ti nanosheets. The scale bars denote a length of 100 nm for the low-magnification (top) and 10 nm for the high-magnification TEM/STEM micrographs (bottom).

empty adsorption site. The occupancy is a measure how densely particles or molecules pack on a surface and how this might affect physico-chemical properties of the surface and the interaction with bacteria. In case of the flat surface the limit of occupancy, or jamming limit, is $\theta_\infty = 0.545$,[18] while for the studied Ti surface jamming limit is lower $\theta_\infty = 0.466$. This means that while the nanostructured surface can accommodate more proteins due to ≈ 4 times increased available area with respect to flat surface, the density of proteins is significantly lower due to curvature of the nanostructures, especially at the bottom of the valleys, Figure 3D top view: nanofeature geometry result convex geometries lead to higher distance between proteins, and hence lower degrees of surface coverage per unit area and correspondingly for concave shapes there are less distances between the proteins and more surface coverage. As a result, there are more proteins on the tips of the nanofeatures than in the valleys. These properties became more pronounced when a decrease in the size mismatch between the proteins and the surface nanostructures occurred.

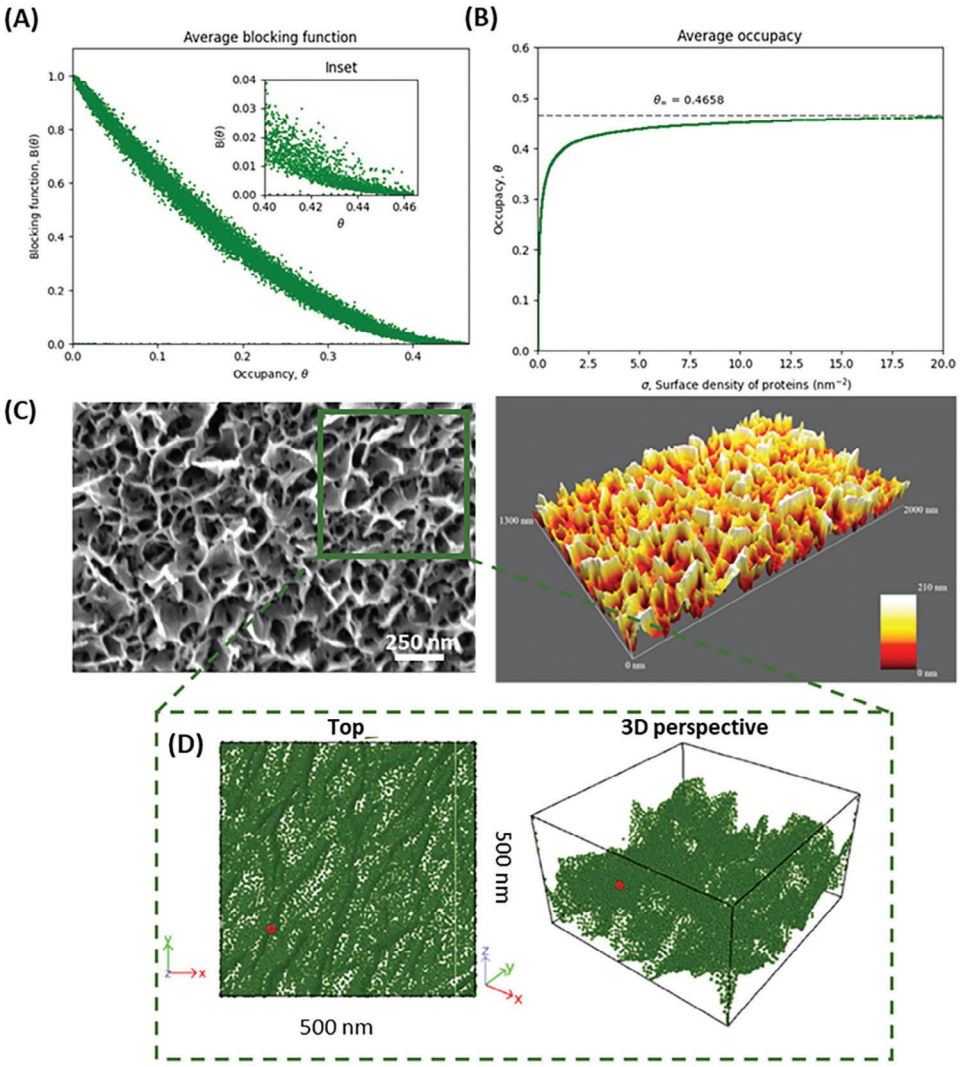

Figure 3. RSA modelling of protein adsorption to HTTi surface at the maximum protein load (saturation limit in RSA model). A) Average blocking function as a function of occupation number of protein on the surface. B) Occupation number versus surface density of proteins. The surface is 500 × 500 nm^2 in projection. The surface area increase due to nanostructures elevation is 4-fold. The protein diameter is 7 nm. C) SEM micrograph and corresponding 3D visualisation of the surface based on SEM used to model serum protein adsorption. D) 3D renders of the protein occupation of the HTTi surface: Top, 3D perspective. Red point shows the reference in all projections. There is more protein adhered at the tip of the nanosheets than in the valleys due to concave shape of the surface.

2.4. Bactericidal Efficacy of HTTi Surfaces with Adsorbed HSP

The sharp edges of the nanosheets produced via hydrothermal treatment have been previously reported to efficiently kill clinically relevant bacterial strains such as Gram-negative *P. aeruginosa* and Gram-positive *S. aureus*, including methicillin resistant strains (MRSA) with efficacy of up to 99%.[12,14] Additionally, a similar surface was able to support the attachment and proliferation of MG-63 osteoblast-like cells despite being infected with bacteria.[31] The bactericidal mechanism of nanosheet-like surfaces is reported to be due to stretching of bacterial cell membrane and cutting the bacterial membrane by physical insertion of the sharp edge of the nanosheet.[40] However, despite the excellent antibacterial efficiency of such nanostructures, it remained unclear whether the mechano-bactericidal activity might be affected by the presence of an adsorbed protein layer. Therefore, we assessed the bactericidal performance of HTTi surfaces with different amounts of adsorbed HSP toward *S. aureus* and *P. aeruginosa*bacteria using staining confocal laser scanning microscopy (CLSM) images (**Figure 4**). Nanostructured surfaces conditioned with HSP protein were hereafter denoted as HTTi+HSP. Assessment of the bactericidal efficacy of HTTi surfaces prior to HSP adsorption was also performed, and it is shown in Figure S5 (Supporting Information). HSP-free HTTi surfaces were able to eliminate *S. aureus* and *P. aeruginosa* bacterial cells with a maximum antibacterial efficiency of 86.6 ± 7% and 95.3 ± 3%, respectively. For comparison, non-structured control surfaces prior to (pTi) and after HSP adsorption (pTi+HSP) were also analysed. On control surfaces, both bacterial cell strains successfully proliferated and thrived, with around 90% of

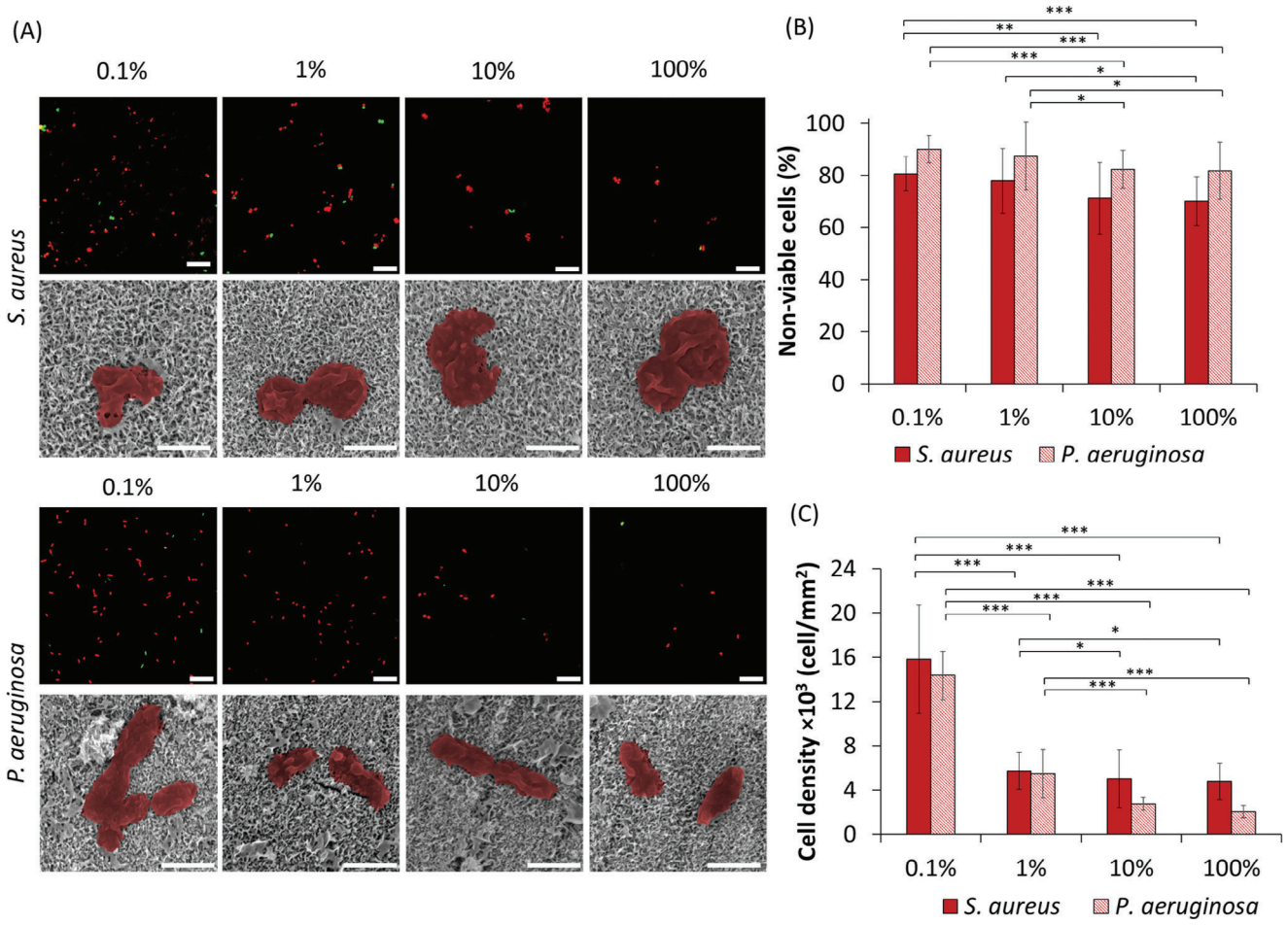

Figure 4. Antibacterial efficacy of HTTi surfaces after HSP adsorption (HTTi+HSP). A) Representative CSLM and SEM micrographs. Typical CLSM micrographs of attached bacteria on nanostructured surfaces showing the proportion of live (green colour) and dead (red colour) bacterial cells. Scale bar = 10 µm. High-magnification SEM images (top view) of *S. aureus* and *P. aeruginosa* cells attached to nanostructured surfaces. The cells exhibited significant levels of altered morphology (highlighted red) when in contact with nanostructured surfaces. Scale bar = 1 µm. B) Bactericidal efficiency presented as a percentage of non-viable bacterial cells. C) Bacterial cell density expressed by the total number of cells adherent per mm^2. Statistically significant differences are labelled as *($p < 0.05$); **($p < 0.01$); ***($p < 0.001$).

bacterial cells alive, as illustrated in Figures S5 and S6 (Supporting Information).

Nanostructured HTTi surfaces with absorbed HSP (HTTi+HSP) demonstrated significant efficacy in eradicating pathogenic *S. aureus* cells. The elimination rates were 80.6 ± 7%, 77.9 ± 12%, 71.1 ± 14%, and 70.1 ± 9% at HSP concentrations of 0.1%, 1%, 10%, and 100%, respectively. In the case of Gram-negative *P. aeruginosa* cells, HTTi+HSP surfaces exhibited remarkable antibacterial activity, eliminating 90.1 ± 5%, 87.4 ± 13%, 82.3 ± 7%, and 81.7 ± 11% of bacterial cells at corresponding HSP concentrations of 0.1%, 1%, 10%, and 100%. The reduced killing efficiency when compared to protein-free HTTi surfaces (Figure S5, Supporting Information) may be associated with the formation of protein aggregates on top of the nanosheets, resulting in an increased nano-edge thickness and reduced sharpness, impairing their mechano-bactericidal efficiency. Despite the reduction in killing efficiency, the surfaces remained highly mechano-bactericidal.

Remarkably, HSP-conditioned HTTi (HTTi+HSP) surfaces exhibited an increased antibiofouling behaviour, with a significant reduction of attached bacterial cells for both strains when compared to protein-free HTTi surfaces. The antibiofouling capacity of the protein layer was more evident at higher HSP concentrations (Figure 4C). Specifically, the attachment propensity of *S. aureus* cells on the nanostructured surfaces was reduced from 46.7 ± 7 × 10^3 cells mm^{-2} (protein-free HTTi surfaces, Figure S5B, Supporting Information) to 16.5 ± 2 × 10^3, 6.5 ± 2 × 10^3, 5.1 ± 2 × 10^3, and 4.8 ± 2 × 10^3 cells mm^{-2} for HTTi+HSP surfaces with HSP concentrations of 0.1%, 1%, 10%, and 100%, respectively (Figure 4C). This reduced attachment accounted for an ≈ 3-fold and 7-fold decrease in attached *S. aureus* cells on the nanostructured surfaces incubated with 0.1% and 1% serum, respectively, and an ≈ 9-fold reduction in attached *S. aureus* cells on surfaces incubated with 10% and 100% HSP concentrations. For *P. aeruginosa* cells, the attachment propensity on the nanostructured surfaces was reduced from 40.2 ± 7 × 10^3 cells mm^{-2} (protein-free HTTi, Figure S5B, Supporting

Information) to 14.4 ± 2 × 10^3, 5.5 ± 2 × 10^3, 2.8 ± 1 × 10^3, and 2.0 ± 1 × 10^3 cells mm^{-2} for HSP concentrations of 0.1%, 1%, 10%, and 100%, respectively. This reduction accounted for 3-, 9-, 15-, and 20-fold reductions in the number of cells attached on surfaces incubated with HSP at concentrations of 0.1%, 1%, 10%, and 100%, respectively. The antibiofouling phenomenon may be explained by the high concentration of albumin in human serum accounting for ≈60% of all protein found in serum.[32] Previous studies have shown that albumin reduced bacterial attachment propensity, especially toward bacteria of the *Staphylococcus* genus.[41] In this work, we also observed antibiofouling behaviour for *P. aeruginosa* cells.

2.5. Competitive Colonization between *S. aureus* and RAW 264.7 macrophage Cells on HTTi Surfaces

Once an implantable device is incorporated into the host, it is believed that both host cells and bacteria attempt to attach to the surface of implant material.[42] If the host cells will be able to colonise the surface first, the bacteria will fail to colonise the surface. Unfortunately, bacterial cells are often colonising the implantable surfaces faster than the host cells.[22a,43] Implant-related infections may be initiated during the implant surface during surgery, thus undermining the tissue integration.[44] In the case of an implanted biomaterial pre-infected with pathogenic bacteria prior to implantation, macrophages work as a part of the innate immune system phagocyting foreign microorganisms, being the primary line of defence of the immune system against pathogens infecting the implanted surface.[45] Macrophages can remain present at the implantation site from weeks to months, exerting crucial biological actions that lead to wound healing.[4b,46]

S. aureus stands as the leading pathogen implicated in infections associated with orthopedic implants, contributing to approximately two-thirds of all bacterial infections occurring in the context of orthopedic implant procedures.[47] Therefore, we assessed the response of RAW 264.7 macrophages to HTTi and HTTi+HSP surfaces pre-infected with *S. aureus* cells. Analysis of RAW 264.7 cell viability during the co-colonization with *S. aureus* revealed no evident cytotoxicity, with cell viability greater than 90% for all analysed samples (**Figure 5**D; Figure S7D, Supporting Information). In the presence of *S. aureus*, the control pTi and pTi+HSP samples showed a progressive decrease in macrophage attachment over the 7 days, regardless of cell viability and HSP adsorption, as seen in Figure 5E and Figure S7E (Supporting Information).

Examination of SEM micrographs showed that the *S. aureus* cells attached to the HTTi and HTTi+HSP surfaces exhibited notably altered bacterial cell morphologies, indicating disrupted cell integrity (Figure 5F; Figure S7F, Supporting Information). In contrast, the bacterial cells attached to pTi and pTi+HSP surfaces were found to possess a smooth and consistent spherical morphology, indicating that the bacterial cells remained healthy once attached to the non-structured surfaces.

The bactericidal efficacy of the HTTi nanosheet topography was assessed with (Figure 5A) and without (Figure S7A, Supporting Information) HSP adsorption, and after 24 h of co-colonisation with RAW 264.7 cells. Analysis of our data showed that HTTi and HTTi+HSP samples killed 79.1 ± 11% and 72.8 ± 9.2% of bacterial cells, respectively (Figure 5A; Figure S7A, Supporting Information). Contrastingly, the control pTi and pTi+HSP samples showed negligible bactericidal potential, with only 10.6 ± 5% and 9.4 ± 4% *S. aureus* cells killed (Figure 5A; Figure S7A, Supporting Information). On day 1 of the in vitro infection model, HTTi+HSP exhibited an *S. aureus* cell density of 148.4 ± 38 cells mm^{-2} compared to 800.2 ± 171 cells mm^{-2} found on pTi+HSP surfaces. This reduction represents a 5-fold decrease in *S. aureus* cell density. A similar correlation can be drawn when comparing surfaces without HSP adsorption. HTTi demonstrated an *S. aureus* cell density of 468.3 ± 164 cells mm^{-2} contrasting to 1260.6 ± 368 cells mm^{-2}, indicating a 3-fold decrease in *S. aureus* cell density. On day 4, no bacterial cells were observed attached to the HTTi and HTTi+HSP surfaces; in contrast, the bacterial cells attached to the control samples (pTi and pTi and HSP) continued to proliferate, resulting in increasing numbers over the 7 days of analysis (Figure 5B; Figure S7B, Supporting Information).

2.6. Phagocytosis by RAW 264.7 Cells

During the first day of co-colonization, the macrophage cells attached to the different Ti surfaces exhibited the formation of phagosomes, as shown in the high resolution CLSM images (**Figure 6**B; Figure S8, Supporting Information). Phagocytosis is illustrated in Figure **6**A, showing macrophage cells engulfing bacterial pathogens. After 4 and 7 days of incubation, the macrophage cells adherent to nanostructured surfaces (HTTi and HTTi+HSP) displayed a rounded morphology, without cytoplasmic membrane extensions (Figure S8, Supporting Information) —In contrast to the nanostructured surfaces, macrophages attached to the control surfaces (pTi and pTi+HSP) exhibited clear and evident phagosomes during the 7 days of analysis, showing enhanced cell area and aspect ratio (Figure **6**D and E; Figure S8, Supporting Information), indicating an active phagocytosis process characteristic of M1 polarized macrophages.[48] In the acute phase of FBR, the macrophages generally exist as the classically activated type 1 (M1) phenotype, characterized by a high expression of pro-inflammatory cytokines and persistent inflammation.[8,49]

TEM/STEM analysis was also performed to investigate the bio-interface and the cell-material interactions between macrophages RAW 264.7 and *S. aureus* cells during competitive colonisation of Ti surfaces. Following 1 day of co-culture, infected Ti samples with attached RAW 264.7 cells were fixed and embedded in a thin layer of resin applied to the disc surface. Thus, subsequent sectioning of the interface revealed an accurate representation of macrophage behaviour at the modified Ti interface. TEM/STEM images revealed large amounts of *S. aureus* engulfed by RAW 264.7 cells on control surfaces prior to (pTi) and after HSP adsorption (pTi+HSP), suggesting an active phagocytosis process (Figure 6C; Figure S9, Supporting Information). By contrast, cross-sectional TEM/STEM analysis of macrophages attached to pre-infected nanostructured surfaces (HTTi and HTTi+HSP) exhibited reduced phagocytic activity (Figure 6C; Figure S9, Supporting Information).

The production of reactive nitrogen species, including nitric oxide, are involved in the antimicrobial activity of macrophages

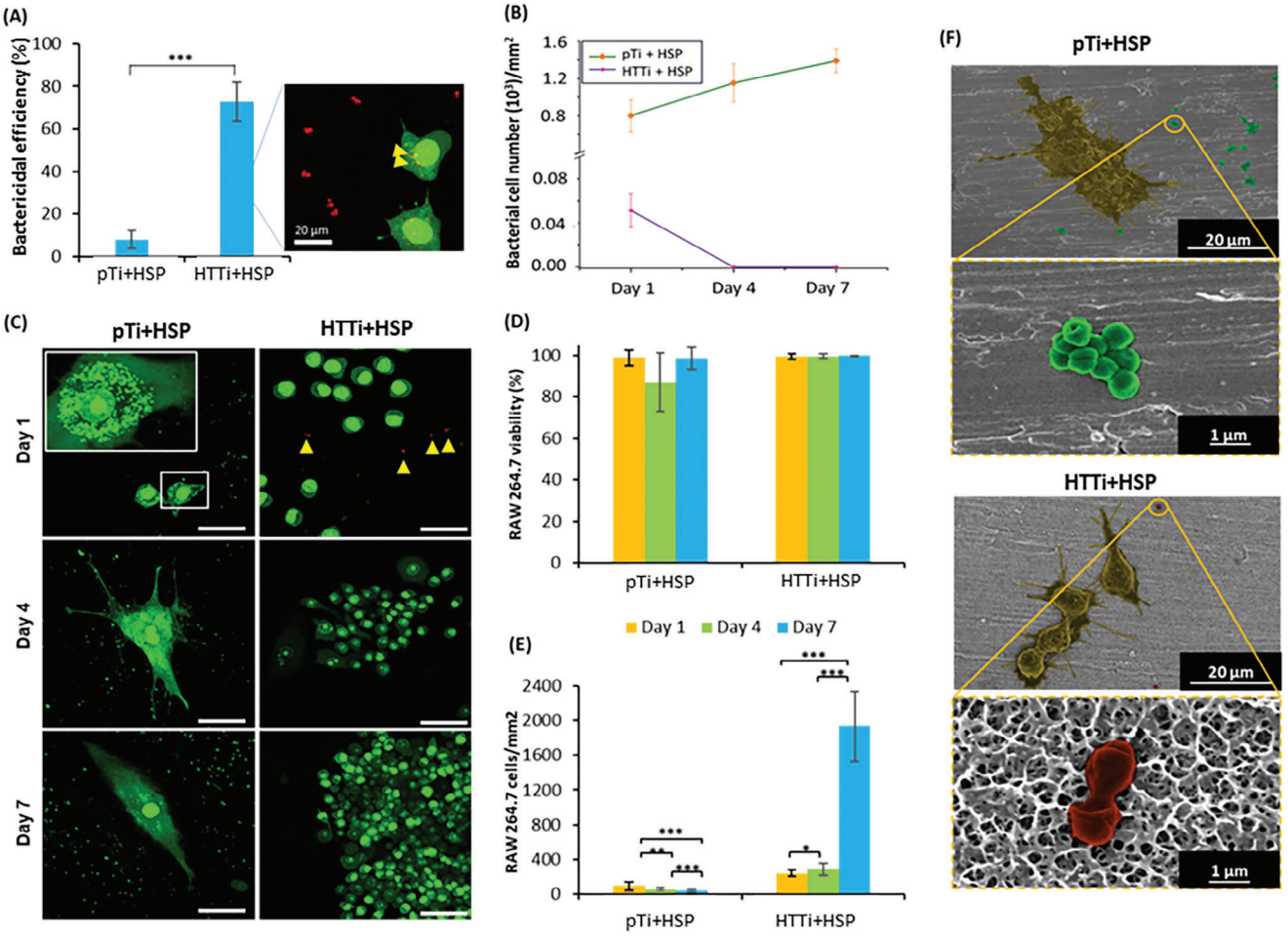

Figure 5. RAW 264.7 cell response to Ti surfaces conditioned with HSP in the presence of an active *S. aureus* infection. A) High antibacterial efficacy of HTTi surfaces during co-colonisation with macrophages. B) Elimination of *S. aureus* cells after 1, 4, and 7 days incubation with macrophages. C) CLSM micrographs of attached RAW 264.7 and *S. aureus* cells on pTi+HSP and HTTi+HSP surfaces. Scale bar = 50 µm. D) RAW 264.7 cell viability during a 7-day incubation period on infected Ti surfaces. E) RAW 264.7 cell number expressed per mm^2. F) SEM images of macrophage and bacteria co-colonisation. *S. aureus* cells exhibit significant levels of altered morphology (highlighted red) when in contact with nanostructured substratum. In contrast, a healthy cell morphology (highlighted green) is observed for control substrata.

toward pathogenic microorganisms.[50] During active infections, macrophages increase the production of nitric oxide as a cytotoxic strategy to eliminate invaders.[51] The large production of nitric oxide by macrophages has been previously related with sepsis.[51a,52] Therefore, the amount of nitric oxide released was assessed by measuring the concentration of nitrite (stable degradation of nitric oxide) in the supernatant of RAW 264.7 cells co-cultured with *S. aureus* cells using Griess Reagent (Figure 6F). The results showed decreased levels of nitric oxide release on HTTi and HTTi+HSP surfaces when compared with that obtained on the pTi and pTi+HSP surfaces. This result agrees with the estimated bactericidal efficiency of HTTi and HTTi+HSP surfaces (Figure 5A; Figure S7A, Supporting Information) and their antibiofouling behaviour (Figure 5B; Figure S7B, Supporting Information) whereby the modified surfaces demonstrated a decreased viability and attachment of *S. aureus* cells. Therefore, it stands to reason that the macrophages released a moderate amount of nitric oxide as a response against the reduced number of viable *S. aureus* cells attached to the HTTi and HTTi+HSP surfaces. In contrast, for the control surfaces (pTi and pTi+HSP), the macrophages cells produced a more severe response against the pathogenic cells, with an increased nitrite concentration being observed.

2.7. Macrophage Polarization on *S. aureus* Infected Ti Surfaces

Inflammation associated with implanted biomaterials and potential wound healing is especially coordinated by macrophages and their polarization conditions. Macrophages exhibit different phenotypes in response to environmental signals.[49,53] In an infection scenario, macrophages polarize to the M1 phenotype and release reactive species (including nitric oxide) as a strategy to assist the host against pathogens.[51,54] Pro-inflammatory M1 macrophages are induced by IFN-γ and lipopolysaccharide and generally express IL-1β, IL-6, iNOS,

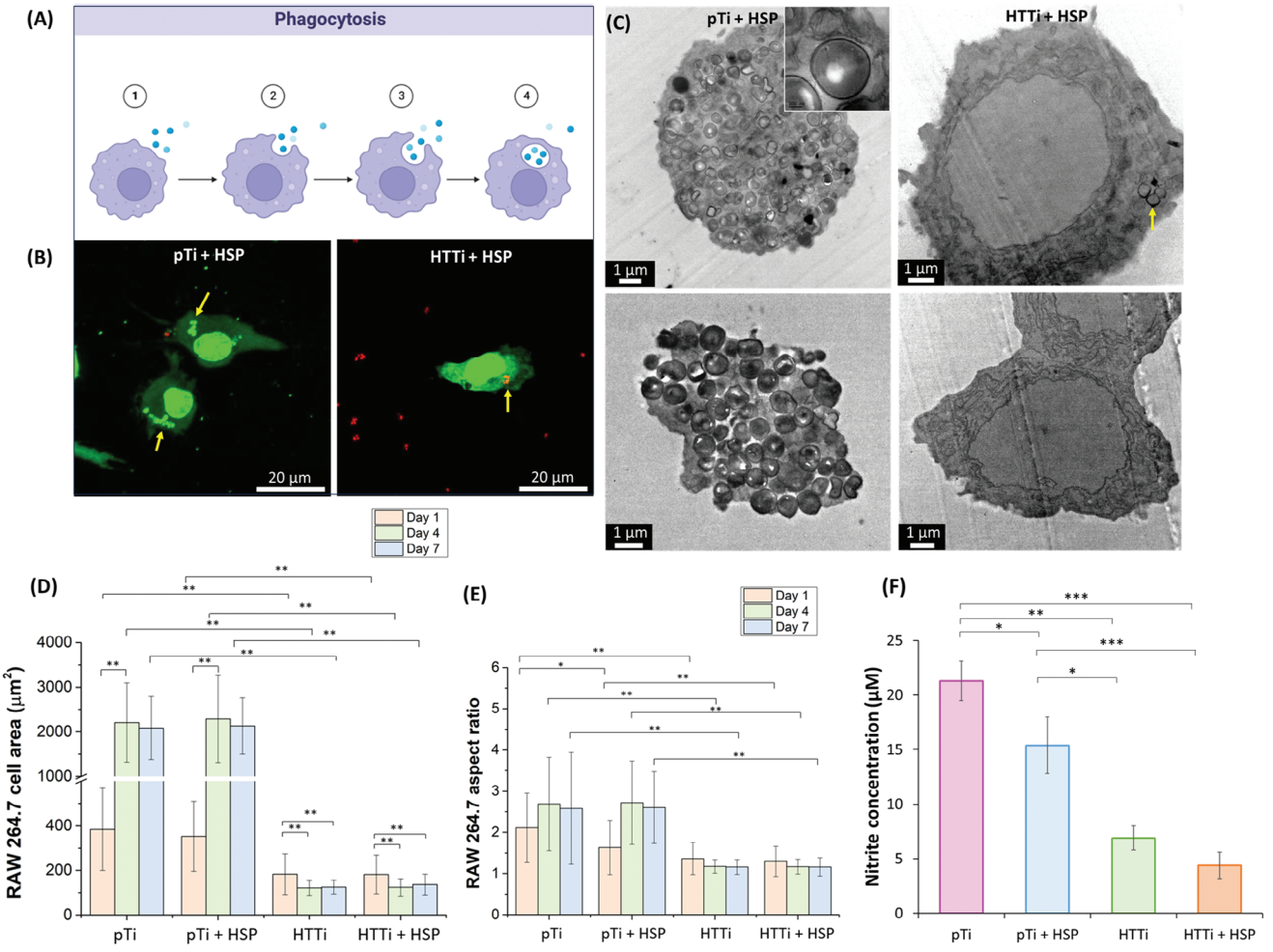

Figure 6. Phagocytosis of *S. aureus* by RAW 264.7 cells during co-colonization. A) Schematic representation of phagocytosis of bacteria by macrophage cells. Created with BioRender.com. B) CLSM micrographs showing RAW 264.7 cells attached to HTTi+HSP and pTi+HSP phagocyting *S. aureus* bacterial cells (yellow arrows). C) TEM/STEM images of RAW 264.7 macrophage cells during co-colonization with *S. aureus* cells. A greater degree of phagocytic activity of RAW 264.7 cells were found on pTi+HSP substrata, revealed by the increased amounts of *S. aureus* cells found engulfed by the macrophages. In contrast, a reduced phagocytic activity on HTTi+HSP surfaces is observed. D,E) Quantification of RAW 264.7 cell morphology including (D) cell area and (E) cell aspect ratio during co-colonization. RAW 264.7 cells attached to infected pTi and pTi+HSP surfaces exhibited enhanced cell area and aspect ratio, characterized by superior phagocytic activity. By contrast, RAW 264.7 cells attached to infected HTTi and HTTi+HSP surfaces did not show significant elongation (aspect ratio of 1.5). F) Relative amounts of nitric oxide production by RAW cells on each Ti surface in the presence of active *S. aureus* infection.

and TNF-α with surface markers CD86 and CCR7.[48,53,55] In contrast, anti-inflammatory M2 macrophages are induced by IL-4/IL-13, IL-10, and immune complexes. M2-activated macrophages produce high levels of ARG1 and IL-10 with surface markers CD163 and CD206 [56] During the transition to the chronic phase of FBR, macrophages switch polarization to the alternatively activated type 2 (M2) phenotype which is associated with the expression of anti-inflammatory cytokines to reduce inflammation and initiate tissue repair and wound healing.[49,57] The presence of a greater proportion of M1 to M2 macrophages is highly indicative of implant failure. Chronic FBR elicited by M1 macrophages impairs osseointegration, leading to eventual osteolytic loosening of the implanted device.[8,49,51c]

RAW 264.7 macrophage polarization on Ti surfaces in the presence of a *S. aureus* infection was investigated by evaluating the expression of M1 and M2 biomarkers—CCR7 and CD206, respectively, and by evaluating the expression of pro-inflammatory (TNF-α and IL-1β) and anti-inflammatory cytokines (IL-4 and IL-10). Macrophages attached to pTi and pTi+HSP surfaces exhibited an upregulated expression of pro-inflammatory biomarkers and cytokines, while cells grown on nanostructured HTTi and HTTi+HSP surfaces demonstrated a significant reduction in pro-inflammatory cytokine expression (**Figures** 7B and C). Moreover, macrophages attached to pTi and pTi+HSP surfaces showed suppressed expression of anti-inflammatory markers and cytokines, while cells grown on HTTi and HTTi+HSP surfaces exhibited an upregulation of anti-inflammatory markers

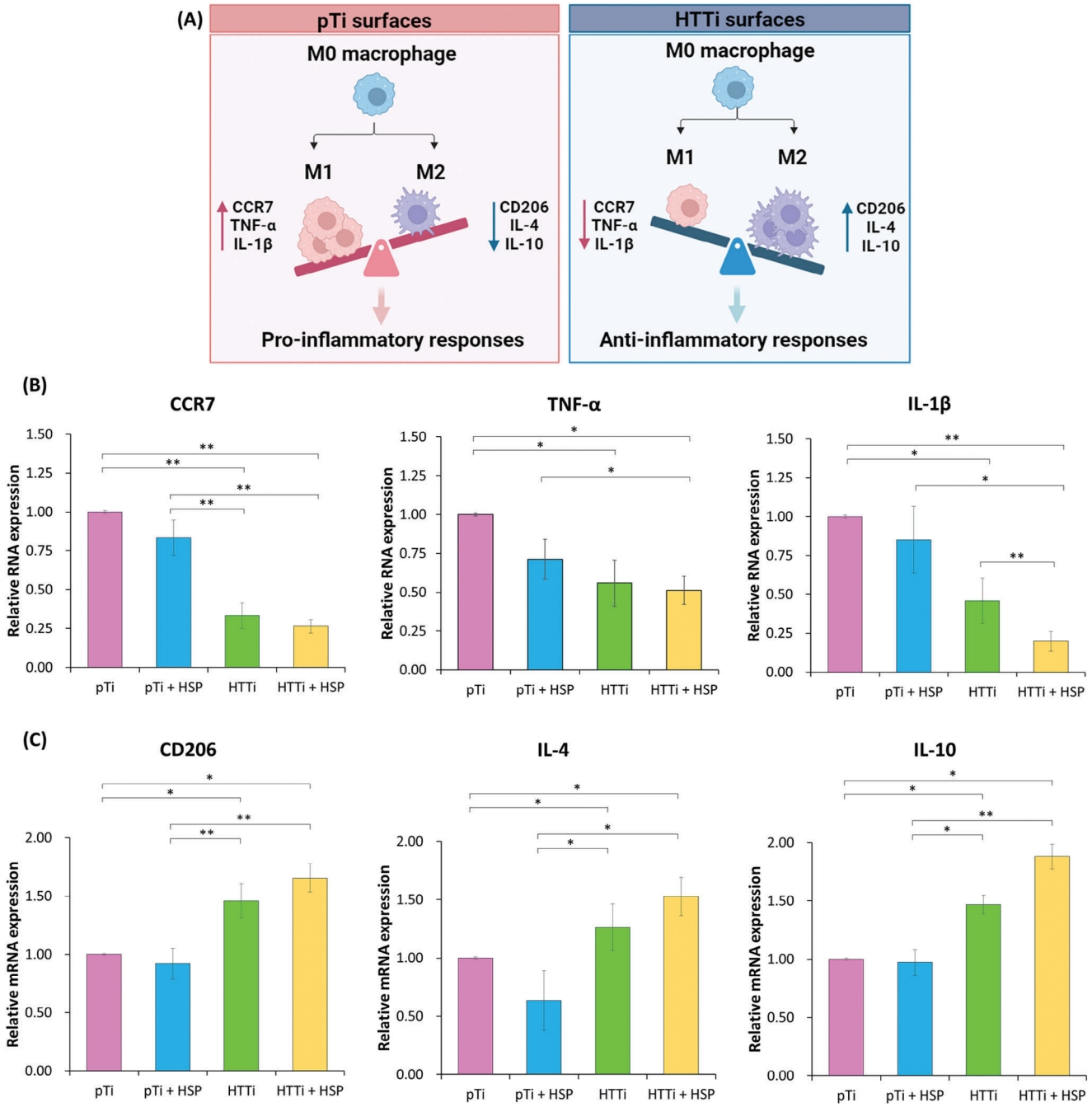

Figure 7. Polarization of RAW 264.7 macrophage during colonisation of pre-infected Ti surfaces with *S. aureus* cells. A) Schematic representation of M1 and M2 macrophage polarisation. When M2 macrophage polarization outweighs M1, a desirable anti-inflammatory response is mediated. Created with BioRender.com. B,C) Expression of relevant pro-inflammatory (B) and anti-inflammatory (C) markers and cytokines evaluated via qPCR.

and cytokines. These results indicated a possible macrophage polarization toward the M1 phenotype on pTi and pTi+HSP surfaces and the M2 phenotype on HTTi and HTTi+HSP surfaces. The data was confirmed with an independent experiment that quantified the production of M1 and M2 biomarkers by fluorescence intensity (Figure S10, Supporting Information). Microplate readings revealed an enhanced M1 biomarker CCR7 fluorescence intensity for RAW 264.7 cells incubated on pTi. In contrast, CCR7 fluorescence intensity was diminished on the HTTi and HTTi+HSP substrata. The opposite trend was observed when evaluating M2 biomarker CD206 fluorescence; macrophages incubated with HTTi and HTTi+HSP exhibited a significant increase in fluorescence intensity compared to that observed on the pTi and pTi+HSP surfaces (Figure S10, Supporting Information). These results indicate that HTTi and HTTi+HSP nanotopography can effectively inactivate

S. aureus bacterial cells while concomitantly inducing the immunomodulation of wound healing associated M2 polarization of RAW 264.7 macrophages cells and reduced inflammatory responses.

3. Discussion

The foreign body response to a biomaterial initiates rapidly following the implantation of a medical device as an inherent consequence of the tissue injury necessary for device placement. The direct contact between blood fluids with the implant surface results in instantaneous adsorption of serum proteins onto the device interface. This protein layer is fundamental to the recruitment of the host immune system that will mediate the fate of implantation. Protein adsorption, however, may also influence the adhesion of pathogenic bacterial cells that contaminate the implant during surgery. Mechano-bactericidal topographies possess highly specific nanopatterns that rely on physical contact between bacteria and the nanofeatures to initiate cell rupture and death. It is well documented that the subtle variations in the geometry of surface nanostructures can significantly impact bactericidal performance.[12e,13c,58] There is ongoing debate that the adsorption of serum proteins to nanostructured surfaces may affect the shape of underlying nanofeatures[18c] and hence, may undermine the mechano-bactericidal performance of the surface. Therefore, the investigation of protein adsorption on mechano-bactericidal surfaces becomes fundamental.

Enhanced adsorption of the antiadhesive serum proteins, such as albumin, is generally reported to hinder osteoblast, macrophages, and bacterial adhesion and proliferation, resulting in a larger anti-inflammatory response and lowered risk of infection but also decreased osseoinduction.[59] It was believed that increased serum protein adhesion to nanostructured surfaces was governed by the increase in surface area alone;[20] however, a recent study proposed that the presence of a highly porous oxide layer on Ti surfaces is the major cause of greater protein adsorption.[31] For example, it was shown by Barberi, et al. that Ti surfaces with significant nanoporosity exhibited a greater level of albumin and fibronectin adsorption compared to flat surfaces.[31] Hydrophobic surfaces have been generally recognized to promote protein adsorption,[38,60] although few research groups have reported an opposite trend, whereby hydrophilic surfaces exhibited augmented levels of protein adsorption.[19]

Herein, our experimental and theoretical analyses clearly indicate that the serum proteins did not occupy the space between the nanofeatures, rather the protein aggregates were formed on the top of the nanofeatures of the HTTi surfaces (Figure 3A). The outcomes of RSA modelling indicated that such pattern of protein adsorption on nanofeatures is due to phenomena associated with the convex geometries of the surface nanofeatures leading to greater distance between proteins, and hence lower degrees of surface coverage per unit area.[18a] Albumin has been documented to aggregate on the top of the nanopillar features.[18]

The bactericidal activity of Ti nanosheets is dependent on the sharpness of the exposed edges.[6,12f] It is important to consider that protein adhesion may lead to an augmented thickness of the nanosheet edges and consequently influence the degree of bactericidal efficacy. Here, however, despite the layer of HSP, the nanotextured surfaces (HTTi+HSP) maintained a high mechano-bactericidal efficacy by killing 81.7 ± 11% and 70.1 ± 9% of *P. aeruginosa* and *S. aureus* cells, respectively. In agreement with previous studies, we showed that the number of *S. aureus* and *P. aeruginosa* cells attached to protein-conditioned hydrothermally treated Ti surfaces (HTTi+HSP) was reduced.[18a,19b,61] Other groups showed that while adsorbed albumin exhibited an antibiofouling toward bacterial attachment, the adsorbed fibronectin was found to promote bacterial attachment.[18a,41,62]

A recent study of bactericidal hydrothermally etched Ti alloy nanospike topography (average height of 348 ± 152 nm, a diameter of 98 ± 60 nm, and spacing of 437 ± 46 nm) demonstrated a killing efficiency of 94.7% of attached *P. aeruginosa* and 61% of attached *S. aureus*.[20] The nanospike topography did not show cytotoxicity toward macrophage cells. The activation state and degree of activation of macrophages grown on various surfaces are highly dependent on the dimensional features of the surface topography and architecture.[63] A comparison of macrophage response to TiO_2 NTs surfaces demonstrated that nanoscale features (<100 nm) are more effective at facilitating M2 polarization than microscale features.[7] So far, the influence of the different nanoscale features and architecture on macrophage polarization, such as nanowires, nanopillars, or nanosheets, has not been clearly defined.[63,64] For example, hydrothermally etched Ti nanowires of different aspect ratio, hence different elastic moduli, were shown to control the polarization of macrophages depending on their ability to deflect in response to cell attachment. Nanostructures with low elastic moduli contributed to enhanced cell spreading and polarization toward the M1 phenotype whereas nanostructures with a high elastic moduli were not conducive to macrophage spreading and resulted in a decreased immune response.[64] A nanoplatelet topography (similar to nanosheets) induced the pro-inflammatory M1 macrophage polarization.[63] Herein, the bactericidal nanosheet topography of the HTTi and HTTi+HSP surfaces positively influenced RAW 264.7 cell attachment, without any detriment to cell viability: the increased number of focal adhesion sites expressed on macrophages colonizing HTTi and HTTi+HSP surfaces suggest that the nanoscale features act as binding sites, favoring the increased adhesion and proliferation of macrophages. We hypothesize that the ability of the nanosheet topography to significantly promote M2 macrophage polarization can be attributed to a combination of serum protein adsorption and topographical factors.

Nevertheless, it is not the quantity of adsorbed protein that dictates the host body response, but the type of protein.[65] For example, it was demonstrated that serum proteins on HTi surfaces adsorbed an increased amount of protein and, in particular, a greater percentage of vitronectin and a decreased amount of complement proteins than nonstructured Ti surfaces (+3% lipoproteins, +4% vitronectin, −8% albumin). THP-1 monocytes attached to the Ti nanospike topography with adsorbed protein demonstrated a significant reduction in pro-inflammatory cytokines and an increase in the production of anti-inflammatory cytokines.[66] Thus, the increased adsorption of fibronectin and vitronectin may play a role in inducing macrophage anti-inflammatory cytokine expression whereas the adsorption of immunoglobulins (IgG) results in the macrophage polarization to

the M1 phenotype and enhanced expression of pro-inflammatory cytokines.[67]

Our in vitro infection model demonstrated that the mechano-bactericidal effect of the HTTi and HTTi+HSP nanosheet topography ensured the rapid elimination of contacting *S. aureus* cells. Macrophages attached to HTTi and HTTi+HSP nanosheet topography did not exhibit an exacerbated phagocytosis (Figure 6), and bacterial cells were not evident on the surface at day 7, suggesting complete early elimination of the infection. In the infection model, macrophages attached to HTTi and HTTi+HSP demonstrated polarization toward the M2 phenotype, revealed by the increased levels of CCR7 and CD206 biomarkers and anti-inflammatory cytokines IL-4 and IL-10. In contrast, the bacterial cells attached to the pTi surfaces successfully proliferated. Macrophages on pTi and pTi+HSP surfaces were observed to be actively phagocytosing *S. aureus* cells but could not out-compete the cells for colonization of the surface over a 7-day incubation period. Bright et al., demonstrated that *S. aureus* cells exhibited a downregulation of capA, which codes for a capsular biosynthesis protein, on a HTTi surface, suggesting that *S. aureus* were less able to produce a capsule and more likely to be recognized and engulfed by macrophages.[68,69] M1 polarization of the RAW 264.7 cells was more evident for pTi and pTi+HSP surfaces. A crucial aspect to ensuring the prolonged and successful biomaterial implantation and efficacy is that the biomaterial should induce desirable immunological responses, facilitating the process of tissue regeneration and macrophages are a key innate immune cell involved in this process.[69]

4. Conclusion

A thorough topographical analysis indicated that the adsorption of a protein layer resulted in an increase in the thickness of the nanosheets on HTTi surfaces, and at increased protein concentrations, the formation of nanoaggregates of protein on top of the nanofeatures; however, without building up the space between the nanosheets as also confirmed by random sequential adsorption modelling. Computer simulation analysis indicated that proteins adhered at the tip of the nanosheets rather than in the valleys due to concave shape of the surface nanofeatures. A detailed evaluation of bactericidal efficiency and bacterial cell attachment showed that, when compared to protein-free nanostructured surfaces (HTTi), the HTTi+HSP killing efficiency was reduced concomitantly with increased adsorbed protein concentrations, perhaps because of the increased thickness and subsequent reduced sharpness of the nanoedges. Nevertheless, the thickness of the nanoedges in the presence of total serum did not exceed ≈ 20 nm, thus allowing the surfaces to maintain high mechano-bactericidal efficacy. Most importantly, the surfaces incubated with HSP demonstrated antibiofouling behaviour when compared to that of the HSP-free surfaces. Here we showed that *S. aureus* infected mechano-bactericidal nanostructured surfaces with a conditioning layer of adsorbed serum protein (HTTi+HSP) positively impacted the inflammatory responses of RAW 264.7 cells towards activated type 2 (M2) phenotype and expression of anti-inflammatory cytokines. We have successfully demonstrated the synergistic effect of HTTi and HTTi+HSP surfaces, that possess nanofeatures capable of mechanically rupture and inactivate bacterial cells, while simultaneously induce pro-healing type 2 (M2) macrophage polarization and secretion of anti-inflammatory cytokines. The outcome of this study provides significant insights into the immunomodulatory characteristics of hydrothermally treated Ti nanostructures and their potential application as a future generation of implantable biomaterials.

5. Experimental Section

Materials and Reagents: Commercially pure ASTM Grade 2 Ti rods of 5 mm diameter were obtained from Goodfellow (Huntingdon, England). KOH pellets (85%), absolute ethanol (99%), and acetone (99%) were purchased from Merck (Pty) Ltd. (Bayswater, Australia).

Fabrication of HTTi Surfaces: A Secotom-50 (Struers, Cleveland, United States) instrument was used to cut the Ti rods into discs of 1 mm thickness. Before surface fabrication, the samples were polished using silicon carbide grinding papers with a grit size of P1200 and ultrasonically cleaned in a sequential cycle of acetone, ethanol, and Milli-Q water for a period of 10 min for each cycle. Non-modified Ti discs (pTi) were used as control surfaces. For the fabrication of surface nanostructures, the samples were then subjected to a hydrothermal treatment by immersing them into 1 M KOH solution in a Teflon-lined reactor and heating to 150 °C for 6 h. Afterward, the samples were retained in MilliQ water for 24 h. Then, the modified discs were annealed at 450 °C using a Thermolyne Muffle Furnace (Thermo Fisher Scientific, Waltham, United States) for 4 h. After annealing, the Ti discs were ultrasonically cleaned for 20 min using a 50% ethanol solution and then air dried.

Optical Profilometry: The surface topography of the different Ti samples was examined using a 3D optical profilometer ContourGT-X (Bruker, Billerica, USA). The average roughness was measured on at least 5 different areas of the surface and then averaged. Images were analysed using the ProfilmOnline platform.

AFM: A NanoWizard4 AFM (JPK BioAFM Business, Bruker NanoGmbH, Germany) was used to characterize the surface topography of the substrata. The AFM head was mounted on an upright optical microscope (IX81, Olympus, Japan), and the experiments were carried out on an active vibration isolation table and in an acoustic hood (Accurion, Germany). The scans were performed in air, using an n-type antimony-doped silicon probe (SICON, AppNano, USA) in JPK's Quantitative Imaging (Qi) mode. AFM image analysis was completed using Gwyddion (ver. 2.62).

Wettability: Surface static WCA measurements were performed under ambient conditions using a Phoenix-MT(T) instrument (SEO Co., Suwon, South Korea), which dispensed a droplet of water with a volume of ≈ 2 µL. The images were analysed using ImageJ software (version 1.48). The results were recorded as an average of five separate measurements for each substratum.

SEM: High-resolution scanning electron micrographs of the Ti surfaces were obtained using a Verios 460L XHR SEM (FEI, Hillsboro, USA) operated at 5 kV. The SEM images were analysed using Image J software (version 1.48).

XPS: XPS was performed to investigate the chemical composition of the samples using a Kratos AXIS Supra XPS (Kratos Analytical Ltd., Manchester, United Kingdom) instrument equipped with a monochromatic X-ray source (aluminium Kα, 1486.7 eV) operated at 150 W.

XRD: XRD was performed to evaluate surface crystallinity using a D4 Endeavor (Bruker, Billerica, USA) instrument equipped with Cu-Kα radiation (λ = 0.15406 nm) under ambient conditions. The samples were scanned under ambient conditions over a 2θ range of 30°–85° at a scanning rate of 1° per minute.

Protein Adsorption: Sterile HSP from male AB plasma were obtained from Sigma-Aldrich (Saint Louis, United States), which was diluted in sterile phosphate-buffered saline (PBS, Gibco, Life Technologies, Carlsbad, United States) to different concentrations (0.1%, 1%, 10%, and undiluted at 100%), as described elsewhere.[70] The Ti surfaces were fully immersed into 200 µL of protein solution at each concentration for 1 h at 37 °C. To remove unattached proteins, the samples were gently washed with PBS.

Total Amount of Protein Estimated using BCA Protein Assay: After HSP incubation onto Ti surfaces as described in 2.9, the total amount of protein adsorbed on the samples was quantified using a BCA protein assay (Thermo Fisher Scientific, Waltham, United States), which was prepared according to the manufacturer's instructions. Since albumin was the predominant protein detected in circulating human plasma serum,[32] assessment of the total amount of bovine serum albumin (BSA) adsorbed on Ti surfaces was also conducted. Similar to HSP, BSA was diluted in sterile PBS to different concentrations (0.1%, 1%, 10%, and undiluted at 100%).

TEM/STEM: Ti samples were incubated with HSP, as described in section (Protein Adsorption), using an HSP concentration of 100%. After incubation, the samples were fixed with 2.5% glutaraldehyde for 1 h and subsequently post-fixed with 1.5% potassium ferrocyanide and 1% osmium tetroxide for 1 h. After washing three times, the surfaces were incubated with 1% uranyl acetate overnight at 4 °C. For TEM visualization, samples containing nanostructures were gently scrapped with a stainless-steel blade, and the content was transferred to an Eppendorf tube containing 10 µL of distilled water. The solution was drop-casted unto copper grits. TEM analysis was performed using a JEM-F200 TEM (JEOL Ltd., Akishima, Japan).

Generalized RSA Model for the Adsorption of Human Serum Albumin: The kinetics of protein adsorption for a given bulk concentration n of proteins were commonly expressed through the fraction of covered area θ as a function of time t. It was usually assumed that the adsorption of proteins does not appreciably affect the bulk protein concentration. This serves as a model control parameter, along with the rates of adsorption and desorption, k_a and k_d, respectively. The kinetics of adsorption were described by the following equation:

$$\frac{d\theta}{dt} = k_a\, nB\,(\theta) - k_d\theta \tag{1}$$

Where, $B(\theta)$ was the blocking function, also known as the surface exclusion effect function. This was defined as the probability to adsorb a protein to the surface for a given occupancy θ. For an empty surface, e.g., at the beginning of adsorption, $\theta = 0$ and the blocking function $B(\theta) = 1$. As the surface coverage increases during the adsorption process, $B(\theta)$ decreases as less substrate surface area becomes available for adsorption, and thus the probability of finding an empty adsorption site decreases. Equation (1) describes the transition towards a dynamic equilibrium, which depends on the concentration and on the geometrical features of the underlying surface, which determine the shape of the blocking function.

In general, an analytical solution to the RSA adsorption requires Monte Carlo (MC) simulations of the adsorption to determine the blocking function $B(\theta)$. In the MC simulations, the blocking function $B(\theta)$ at a given coverage θ in the RSA model was defined as the ratio between the number of potentially successful attempts, N_{succ}, and the total amount of attempts, N_{att}.

$$\mathrm{B}\theta = \frac{N_{succ}}{N_{att}} \tag{2}$$

Each system was simulated N times and for each configuration in a given simulation, the number of attempts required to adsorb the particle was computed. Numerically, the calculation was performed with the use of a MC method, which records the number of successful attempts required to attach the protein onto a free site. Each simulation was repeated 1000 times. As a result, the blocking function $B(\theta)$ was computed as an average of the number of attempts for a given surface coverage θ.

Results for equations (1) and (2) were computed for the real nanostructured surface as obtained by AFM. AFM scans were performed in tapping mode on a JPK Nanowizard (Bruker), in air at ambient conditions, using a silicon cantilever (Cont20A, Veeco Probes) with a spring constant of 0.9N m^{-1} and a resonance frequency of ≈20 kHz over a scan area of 0.5×0.5 µm^2.

Bacterial Strains and Growth Conditions: Gram-negative *P. aeruginosa* ATCC 9721 and Gram-positive *S. aureus* CIP 65.8^T bacteria were obtained from the American Type Culture Collection (ATCC, Manassas, United States) and the Collection de l'Institut Pasteur (CIP, Paris, France). Bacterial cells were refreshed from frozen stocks on nutrient agar (Oxoid, Thermo Fisher Scientific, Waltham, United States) for 24 h at 37 °C.

Bacterial Viability and Attachment: At least three independent experiments were completed for each strain, where bacterial cell suspensions were prepared by suspending one or two loopfuls of bacteria in 5 mL of nutrient broth (Oxoid, Thermo Fisher Scientific, Waltham, United States). The cell suspensions were adjusted to an optical density of $OD_{600} = 0.1$ by further dilution with nutrient broth. Sterilized Ti discs were fully immersed in 100 µL of bacterial suspension in a sterile 96-well plate for 18 h at 25 °C under static and dark conditions. After incubation, the samples were gently washed, stained for 25 min using a LIVE/DEAD BacLight Bacterial Viability Kit (Invitrogen, Carlsbad, United States), and imaged via CLSM (Zeiss LSM 880, Carl Zeiss Microscopy, Jena, Germany).

Following the 18 h incubation period, the Ti discs with attached bacterial cells were fixed with 2.5% glutaraldehyde (Sigma-Aldrich, Saint Louis, United States) and sequentially dehydrated with a graded ethanol series (ethanol volume fractions of 30, 50, 70, 90, and 100% for 10 min each). The samples were sputter-coated using a Leica EM ACE600 (Leica Microsystems GmbH, Wetzlar, Germany) with 5 nm of iridium. High-resolution scanning electron micrographs of the Ti surfaces were obtained using a Verios 460L XHR SEM (FEI, Hillsboro, USA) operated at 5 kV. The SEM images were analysed using Image J software (version 1.48).

RAW 264.7 Cell Line: The RAW 264.7 macrophage cell line was purchased from American Type Culture Collection (ATCC, Manassas, United States). The cells were cultured in T75 cell culture flasks with Dulbecco's Modified Eagle Medium (DMEM, Gibco, Life Technologies, Carlsbad, United States) at 37 °C in a humidified incubator with 5% CO_2. The RAW 264.7 cells were sub-cultured when the cell density achieved 90% confluency. Once confluent, the culture medium was removed, and the adherent cells were rinsed with sterile phosphate-buffered saline (PBS, Gibco, Life Technologies, Carlsbad, United States) and trypsinized using Trypsin-EDTA (0.25%) (Gibco, Life Technologies, Carlsbad, United States) at 37 °C for 3 min. Then, the cell suspension was centrifuged at 250 RCF for 5 min. Following centrifugation, the supernatant was removed, and the resultant cell pellet was resuspended in 1 mL of DMEM.

The Ti discs were placed in a sterile 96-well plate and then fully covered with a suspension of RAW 264.7 cells at a density of 5×10^3 cells mL^{-1} and incubated at 37 °C in a humidified atmosphere incubator with 5% CO_2. The incubation periods used for analysis were 1, 4, and 7 days.

RAW 264.7 Cell Viability and Attachment: Ti discs with attached RAW 264.7 cells, as described in 2.15, were stained with calcein AM (2 µM) and ethidium homodimer-1 (4 µM) (Invitrogen, Carlsbad, United States) for 30 min under dark conditions at room temperature. The samples were subsequently imaged using CLSM (Zeiss LSM 880, Carl Zeiss Microscopy, Jena, Germany).

Immunocytochemistry and Cytoskeleton Staining: Ti discs seeded with RAW 264.7 cells were washed twice with PBS and subsequently fixed using 4% paraformaldehyde for 15 min. The cells were permeabilized using 0.2% Triton X-100 for a further 15 min. Following this, the cells were blocked in 1% BSA for 30 min. The cells were then treated with an anti-vinculin (mouse) primary antibody as an indicator of focal adhesions at room temperature for 1 h. A secondary antibody, anti-Mouse IgG in goat serum, was drop-cast onto samples and incubated for 1 h at room temperature; the actin filaments were stained using phalloidin for a further 20 min, and then the cell nuclei were stained using TO-PRO−3 Iodide for 30 min. The cells were imaged using CLSM (Zeiss LSM 880, Carl Zeiss Microscopy, Jena, Germany).

Competitive Colonization in vitro Model: Gram-positive *S. aureus* CIP 65.8T bacteria were obtained from the Collection de l'Institut Pasteur (CIP, Paris, France). The bacterial cells were refreshed from frozen stocks on nutrient agar (Oxoid, Thermo Fisher Scientific, Waltham, United States) for 24 h at 37 °C. The cell suspensions were adjusted to an infective dose of 10^5 cells per mL, as previously described.[22] Sterilised Ti discs were fully immersed in 100 µL of bacterial suspension in a sterile 96-well plate for 6 h at 25 °C under static and dark conditions. After pre-infection,

the RAW 264.7 cell line was prepared in a penicillin-streptomycin-free DMEM and were seeded on pre-infected Ti surfaces at a density of 5×10^3 cells mL^{-1} and incubated at 37 °C in a humidified atmosphere incubator with 5% CO_2. The competitive colonization was assessed at 1, 4, and 7 days. After the co-colonization incubation period, the samples were gently washed, stained using a LIVE/DEAD BacLight Bacterial Viability Kit (Invitrogen, Carlsbad, United States), and with calcein AM (2 µM) and ethidium homodimer-1 (4 µM) (Invitrogen, Carlsbad, United States) for 30 min under dark conditions at room temperature. The samples were imaged using CLSM.

Quantification of Nitric Oxide Production: Nitric oxide release was assessed by a Griess assay (Biotium, San Francisco, United States). RAW 264.7 and *S. aureus* cells were co-colonized as described in the section (Competitive Colonization in vitro Model) for 2 days. After the co-colonization incubation period, the supernatant (150 µL) was collected, mixed with Griess reagent (20 µL), and incubated at room temperature for 30 min as per manufacture protocol. The solution was then transferred to a 96-well plate, and its absorbance at 550 nm was recorded using a CLARIOstar Plus microplate reader (BMG LabTech Pty., Ltd., Ortenberg, Germany).

Quantification of M1 and M2 polarization markers CCR7 and CD206: Ti discs were co-colonized with RAW 264.7 and *S. aureus* cells, as previously described in the section (Competitive Colonization in vitro Model) for 2 days. After co-colonization, the RAW 264.7 cells were trypsinized and washed with PBS. The RAW 264.7 cells were then blocked with CD16/32 for 10 min and subsequently incubated with allophycocyanin-conjugated CCR7 and phycoerythrin-conjugated CD206 for 1 h. After incubation, the cell suspension was transferred to a 96-well plate, and the fluorescence intensity (excitation/emission: 650/660 nm for allophycocyanin and 565/578 for phycoerythrin) was recorded using a CLARIOstar Plus microplate reader (BMG LabTech Pty., Ltd., Ortenberg, Germany).

Macrophage Polarization: Ti samples were seeded with *S. aureus* and RAW 264.7 cells, as described in the section (Competitive Colonization in vitro Model) and incubated for 2 days. After incubation, RNA was extracted using an Isolate II RNA Mini Kit (Meridian Bioscience Inc., Cincinnati, United States) according to the manufacturer's protocol. The total isolated RNA was converted to cDNA using a SensiFAST cDNA Synthesis Kit (Meridian Bioscience Inc., Cincinnati, United States). Finally, a SensiFAST SYBR & Fluorescein Kit (Meridian Bioscience Inc., Cincinnati, United States) was used to quantify the expression of TNF-α and IL-β, as anti-inflammatory cytokines IL-4 and iIL-10, as well as M1 and M2 markers CCR7 and CD206 via a real-time quantitative polymerase chain reaction (RT-qPCR) assay. The sequences of the forward and reverse primers used in this work were collected from previously published work[71] (**Table 1**). Gene expression was normalized to the housekeeping gene (GAPDH). RT-qPCR analysis was performed using a CFX96 Touch real-time PCR detection system (Bio-Rad, Hercules, USA).

Statistical Analysis: All data were presented as mean ± standard deviation, representative of three independent experiments. Statistical analysis was performed using a Student's t-test in GraphPad Prism, where $p < 0.05$ was used to determine statistical significance.

Graphical Illustrations: The graphical illustrations seen in the Graphical Abstract, Figure 6A, and Figure 7A were created using BioRender.com.

Table 1. Primer sequences for real-time PCR analysis.

Gene	Forward sequence (5′-3′)	Reverse sequence (3′-5′)
TNF-α	CCCTCACACTCAGATCATCTTCT	GCTACGACGTGGGCTACAG
IL-1β	TGCCACCTTTTGACAGTGATG	AAGGTCCACGGGAAAGACAC
IL-4	CCATATCCACGGATGCGACA	AAGCCCGAAAGAGTCTCTGC
IL-10	GCTCTTACTGACTGGCATGAG	CGCAGCTCTAGGAGCATGTG
CCR7	TGTACGAGTCGGTGTGCTTC	GGTAGGTATCCGTCATGGTCTTG
CD206	CTCTGTTCAGCTATTGGACGC	CGGAATTTCTGGGATTCACGTTC
GAPDH	AGGTCGGTGTGAACGGATTTG	TGTAGACCATGTAGTTGAGGTCA

Supporting Information

Supporting Information is available from the Wiley Online Library or from the author.

Acknowledgements

Open access publishing facilitated by RMIT University, as part of the Wiley - RMIT University agreement via the Council of Australian University Librarians.

Conflict of Interest

The authors declare no conflict of interest.

Data Availability Statement

The data that support the findings of this study are available in the supplementary material of this article.

Keywords

antibacterial surfaces, human serum proteins adsorption, mechano-bactericidal surfaces, titanium biomaterials

Received: December 8, 2023
Revised: February 4, 2024
Published online: March 14, 2024

[1] a) S.-R. Choi, J.-W. Kwon, K.-S. Suk, H.-S. Kim, S.-H. Moon, S.-Y. Park, B. H. Lee, *Materials* **2023**, *16*, 3633; b) R. Davis, A. Singh, M. J. Jackson, R. T. Coelho, D. Prakash, C. P. Charalambous, W. Ahmed, L. R. R. da Silva, A. A. Lawrence, *Int. J. Adv. Manuf. Technol.* **2022**, *120*, 1473; c) M. Prakasam, J. Locs, K. Salma-Ancane, D. Loca, A. Largeteau, L. Berzina-Cimdina, *J. Funct. Biomater.* **2017**, *8*, 44.

[2] a) D. F. Williams, *Bioact. Mater.* **2022**, *10*, 306; b) E. Madsen, M. Mededovic, D. H. Kohn, *Biochem. Soc. Trans.* **2020**, *48*, 2039.

[3] a) A. Przekora, *Mater. Sci. Eng., C* **2019**, *97*, 1036; b) F. S. Ismail, R. Rohanizadeh, S. Atwa, R. S. Mason, A. J. Ruys, P. J. Martin, A. Bendavid, *J. Mater. Sci. Mater. Med.* **2007**, *18*, 705.

[4] a) F. Batool, H. Özçelik, C. Stutz, P.-Y. Gegout, N. Benkirane-Jessel, C. Petit, O. Huck, *J. Tissue Eng.* **2021**, *12*, 204173142110414; b) J. J. Li, H. Zreiqat, in *Encyclopedia of Biomedical Engineering* (Ed: R. Narayan), Elsevier, Oxford **2019**, p. 270.

[5] a) R. Londono, S. F. Badylak, in *Host Response to Biomaterials* (Ed: S. F. Badylak), Academic Press, Oxford **2015**, Ch. 1, p. 1; b) G. Fumagall, V. Panichi, in *Critical Care Nephrology* (3rd Ed.) (Eds: C. Ronco, R. Bellomo, J. A. Kellum, Z. Ricci), Elsevier, Philadelphia **2019**, Vol. *151*, p. 918.

[6] a) K. M. Hotchkiss, G. B. Reddy, S. L. Hyzy, Z. Schwartz, B. D. Boyan, R. Olivares-Navarrete, *Acta Biomater.* **2016**, *31*, 425; b) M. S. Pitchai, D. S. Ipe, S. Hamlet, *J. Funct. Biomater.* **2023**, *14*, 211.

[7] a) L. Bai, Y. Zhao, P. Chen, X. Zhang, X. Huang, Z. Du, R. Crawford, X. Yao, B. Tang, R. Hang, Y. Xiao, *Small* **2020**, *17*, 2006287; b) Y. Zhu, H. Liang, X. Liu, J. Wu, C. Yang, T. M. Wong, K. Y. H. Kwan, K. M. C. Cheung, S. Wu, K. W. K. Yeung, *Sci. Adv.* **2021**, *7*, 1; c) Y. He, J. Luo, Y. Zhang, Z. Li, F. Chen, W. Song, Y. Zhang, *Mater. Sci. Eng., C* **2020**, *106*, 110221; d) H. Qi, M. Shi, Y. Ni, W. Mo, P. Zhang, S. Jiang, Y. Zhang, X. Deng, *Adv. Healthcare Mater.* **2021**, *10*, 2100994; e) Q.-L. Ma, L.-Z. Zhao, R.-R. Liu, B.-Q. Jin, W. Song, Y. Wang, Y.-S. Zhang, L.-H. Chen, Y.-M. Zhang, *Biomaterials* **2014**, *35*, 9853.

[8] Q.-l. Ma, L. Fang, N. Jiang, L. Zhang, Y. Wang, Y.-m. Zhang, L.-h. Chen, *Biomaterials* **2018**, *154*, 234.
[9] H. Pan, Y. Xie, Z. Zhang, K. Li, D. Hu, X. Zheng, T. Tang, *Biomed. Mater.* **2017**, *12*, 045006.
[10] J. M. Schierholz, J. Beuth, *J. Hosp. Infect.* **2001**, *49*, 87.
[11] a) S. S. Magill, J. R. Edwards, W. Bamberg, Z. G. Beldavs, G. Dumyati, M. A. Kainer, R. Lynfield, M. Maloney, L. McAllister-Hollod, J. Nadle, S. M. Ray, D. L. Thompson, L. E. Wilson, S. K. Fridkin, *N. Engl. J. Med.* **2014**, *370*, 1198; b) J. S. VanEpps, J. G. Younger, *Shock* **2016**, *46*, 597.
[12] a) C. M. Bhadra, V. K. Truong, V. T. H. Pham, M. Al Kobaisi, G. Seniutinas, J. Y. Wang, S. Juodkazis, R. J. Crawford, E. P. Ivanova, *Sci. Rep.* **2015**, *5*, 16817; b) E. P. Ivanova, J. Hasan, H. K. Webb, G. Gervinskas, S. Juodkazis, V. K. Truong, A. H. F. Wu, R. N. Lamb, V. A. Baulin, G. S. Watson, J. A. Watson, D. E. Mainwaring, R. J. Crawford, *Nat. Commun.* **2013**, *4*, 2838; c) D. P. Linklater, M. De Volder, V. A. Baulin, M. Werner, S. Jessl, M. Golozar, L. Maggini, S. Rubanov, E. Hanssen, S. Juodkazis, E. P. Ivanova, *ACS Nano* **2018**, *12*, 6657; d) D. P. Linklater, S. Juodkazis, R. J. Crawford, E. P. Ivanova, *Materialia* **2019**, *5*, 100197; e) D. P. Linklater, H. K. D. Nguyen, C. M. Bhadra, S. Juodkazis, E. P. Ivanova, *Nanotechnology* **2017**, *28*, 245301; f) J. V. Wandiyanto, T. Tamanna, D. P. Linklater, V. K. Truong, M. Al Kobaisi, V. A. Baulin, S. Joudkazis, H. Thissen, R. J. Crawford, E. P. Ivanova, *J. Colloid Interface Sci.* **2020**, *560*, 572.
[13] a) E. P. Ivanova, J. Hasan, H. K. Webb, V. K. Truong, G. S. Watson, J. A. Watson, V. A. Baulin, S. Pogodin, J. Y. Wang, M. J. Tobin, C. Löbbe, R. J. Crawford, *Small* **2012**, *8*, 2489; b) J. Hasan, H. K. Webb, V. K. Truong, S. Pogodin, V. A. Baulin, G. S. Watson, J. A. Watson, R. J. Crawford, E. P. Ivanova, *Appl. Microbiol. Biotechnol.* **2013**, *97*, 9257; c) D. E. Mainwaring, S. H. Nguyen, H. Webb, T. Jakubov, M. Tobin, R. N. Lamb, A. H. F. Wu, R. Marchant, R. J. Crawford, E. P. Ivanova, *Nanoscale* **2016**, *8*, 6527; d) S. H. Nguyen, H. K. Webb, P. J. Mahon, R. J. Crawford, E. P. Ivanova, *Molecules* **2014**, *19*, 13614; e) R. J. Crawford, E. P. Ivanova, in *Superhydrophobic surfaces*, Elsevier, Amsterdam, Netherlands **2015**.
[14] a) D. P. Linklater, V. A. Baulin, S. Juodkazis, R. J. Crawford, P. Stoodley, E. P. Ivanova, *Nat. Rev. Microbiol.* **2021**, *19*, 8; b) J. V. Wandiyanto, S. Cheeseman, V. K. Truong, M. A. Kobaisi, C. Bizet, S. Juodkazis, H. Thissen, R. J. Crawford, E. P. Ivanova, *J. Mater. Chem. B* **2019**, *7*, 4424; c) N. Rawat, M. Benčina, E. Gongadze, I. Junkar, A. Iglič, *ACS Omega* **2022**, *7*, 47070; d) K. Martins de Sousa, D. P. Linklater, B. J. Murdoch, M. Al Kobaisi, R. J. Crawford, R. Judge, S. Dashper, A. J. Sloan, D. Losic, E. P. Ivanova, *ACS Appl. Bio Mater.* **2023**, *6*, 1054.
[15] T. L. Clainche, D. Linklater, S. Wong, P. Le, S. Juodkazis, X. L. Guével, J.-L. Coll, E. P. Ivanova, V. Martel-Frachet, *ACS Appl. Mater. Interfaces* **2020**, *12*, 48272.
[16] a) J. V. Wandiyanto, D. Linklater, P. G. Tharushi Perera, A. Orlowska, V. K. Truong, H. Thissen, S. Ghanaati, V. Baulin, R. J. Crawford, S. Juodkazis, E. P. Ivanova, *Materials* **2018**, *11*, 1; b) C. M. Bhadra, V. Khanh Truong, V. T. H. Pham, M. Al Kobaisi, G. Seniutinas, J. Y. Wang, S. Juodkazis, R. J. Crawford, E. P. Ivanova, *Sci. Rep.* **2015**, *5*, 16817.
[17] Y. Arima, H. Iwata, *J. Mater. Chem.* **2007**, *17*, 4079.
[18] a) L. Zhao, T. Liu, X. Li, Q. Cui, X. Wang, K. Song, D. Ge, *Appl. Surf. Sci.* **2022**, *576*, 151779; b) C. M. Bhadra, M. Werner, V. A. Baulin, V. K. Truong, M. A. Kobaisi, S. H. Nguyen, A. Balcytis, S. Juodkazis, J. Y. Wang, D. E. Mainwaring, R. J. Crawford, E. P. Ivanova, *Nano-Micro Lett.* **2018**, *10*, 36; c) D. H. K. Nguyen, V. T. H. Pham, M. Al Kobaisi, C. Bhadra, A. Orlowska, S. Ghanaati, B. M. Manzi, V. A. Baulin, S. Joudkazis, P. Kingshott, R. J. Crawford, E. P. Ivanova, *Langmuir* **2016**, *32*, 10744; d) B. M. Manzi, M. Werner, E. P. Ivanova, R. J. Crawford, V. A. Baulin, *Sci. Rep.* **2019**, *9*, 4694.
[19] a) L. T. Allen, M. Tosetto, I. S. Miller, D. P. O'Connor, S. C. Penney, I. Lynch, A. K. Keenan, S. R. Pennington, K. A. Dawson, W. M. Gallagher, *Biomaterials* **2006**, *27*, 3096; b) J. Zhong, X. Li, Y. Yao, J. Zhou, S. Cao, X. Zhang, Y. Jian, K. Zhao, *J. Mater. Sci.: Mater. Med.* **2022**, *33*, 20; c) B. S. Kopf, S. Ruch, S. Berner, N. D. Spencer, K. Maniura-Weber, *J. Biomed. Mater. Res., Part A* **2015**, *103*, 2661.
[20] R. M. Visalakshan, R. Bright, A. L. S. Burzava, A. J. Barker, J. Simon, N. Ninan, D. Palms, J. Wood, M. Martínez-Negro, S. Morsbach, V. Mailänder, P. H. Anderson, T. Brown, D. Barker, K. Landfester, K. Vasilev, *ACS Appl. Mater. Interfaces* **2022**, *15*, 220.
[21] D. P. Linklater, S. Juodkazis, E. P. Ivanova, *Nanoscale* **2017**, *9*, 16564.
[22] a) V. T. H. Pham, V. K. Truong, A. Orlowska, S. Ghanaati, M. Barbeck, P. Booms, A. J. Fulcher, C. M. Bhadra, R. Buividas, V. Baulin, C. J. Kirkpatrick, P. Doran, D. E. Mainwaring, S. Juodkazis, R. J. Crawford, E. P. Ivanova, *ACS Appl. Mater. Interfaces* **2016**, *8*, 22025; b) J. V. Wandiyanto, V. K. Truong, M. Al Kobaisi, S. Juodkazis, H. Thissen, O. Bazaka, K. Bazaka, R. J. Crawford, E. P. Ivanova, *Materials* **2019**, *12*, 1575.
[23] J. V. Wandiyanto, D. Linklater, P. G. Tharushi Perera, A. Orlowska, V. K. Truong, H. Thissen, S. Ghanaati, V. Baulin, R. J. Crawford, S. Juodkazis, E. P. Ivanova, *Materials* **2018**, *11*, 605.
[24] C. Kim, M. R. Kendall, M. A. Miller, C. L. Long, P. R. Larson, M. B. Humphrey, A. S. Madden, A. C. Tas, *Mater. Sci. Eng., C* **2013**, *33*, 327.
[25] M.-K. Han, J.-B. Im, M.-J. Hwang, B.-J. Kim, H.-Y. Kim, Y.-J. Park, *Metals* **2015**, *5*, 850.
[26] J. Vishnu, V. K. Manivasagam, V. Gopal, C. Bartomeu Garcia, P. Hameed, G. Manivasagam, T. J. Webster, *Nanomed.: Nanotechnol., Biol. Med.* **2019**, *20*, 102016.
[27] a) D. Salthouse, K. Novakovic, C. M. U. Hilkens, A. M. Ferreira, *Acta Biomater.* **2023**, *155*, 1; b) S. Wang, Y. Chen, Z. Ling, J. Li, J. Hu, F. He, Q. Chen, *Int. J. Oral Sci.* **2022**, *14*, 52.
[28] J.-P. Deville, C. S. Cojocaru, in *Materials Surface Processing by Directed Energy Techniques* (Ed: Y. Pauleau), Elsevier, Oxford **2006**, Vol. *12*, p. 411.
[29] a) P. E. Scopelliti, A. Borgonovo, M. Indrieri, L. Giorgetti, G. Bongiorno, R. Carbone, A. Podestà, P. Milani, *PLoS One* **2010**, *5*, e11862; b) H. Juvonen, A. Määttänen, P. Ihalainen, T. Viitala, J. Sarfraz, J. Peltonen, *Colloids Surf., B* **2014**, *118*, 261.
[30] I. Firkowska-Boden, X. Zhang, K. D. Jandt, *Adv. Healthcare Mater.* **2018**, *7*, 1700995.
[31] J. Barberi, L. Mandrile, L. Napione, A. M. Giovannozzi, A. M. Rossi, A. Vitale, S. Yamaguchi, S. Spriano, *Appl. Surf. Sci.* **2022**, *599*, 154023.
[32] R. N. Moman, N. Gupta, M. Varacallo, in StatPearls, Treasure Island (FL) Physiology, Albumin, StatPearls Publishing LLC **2022**, https://pubmed.ncbi.nlm.nih.gov/29083605/.
[33] N. Kuntip, D. Japrung, P. Pongprayoon, *Biopolymers* **2021**, *112*, e23421.
[34] K. Rechendorff, M. B. Hovgaard, M. Foss, V. P. Zhdanov, F. Besenbacher, *Langmuir* **2006**, *22*, 10885.
[35] T. T. Nguyen, M. Miyauchi, A. M. Rahmatika, K. L. A. Cao, E. Tanabe, T. Ogi, *ACS Appl. Mater. Interfaces* **2022**, *14*, 14435.
[36] a) W. Yang, X. Xi, Q. Ran, P. Liu, Y. Hu, K. Cai, *Mater. Sci. Eng., C* **2014**, *34*, 410; b) Y. Hu, K. Cai, Z. Luo, D. Xu, D. Xie, Y. Huang, W. Yang, P. Liu, *Acta Biomater.* **2012**, *8*, 439.
[37] R. M. Visalakshan, M. N. MacGregor, S. Sasidharan, A. Ghazaryan, A. M. Mierczynska-Vasilev, S. Morsbach, V. Mailänder, K. Landfester, J. D. Hayball, K. Vasilev, *ACS Appl. Mater. Interfaces* **2019**, *11*, 27615.
[38] J. Barberi, S. Spriano, *Materials* **2021**, *14*, 1590.
[39] X. Wu, C. Wang, P. Hao, F. He, Z. Yao, X. Zhang, *Colloids Surf., B* **2021**, *207*, 111994.
[40] V. T. H. Pham, V. K. Truong, M. D. J. Quinn, S. M. Notley, Y. Guo, V. A. Baulin, M. Al Kobaisi, R. J. Crawford, E. P. Ivanova, *ACS Nano* **2015**, *9*, 8458.

[41] a) S. Schuster, W. Yu, M. Nega, Y.-Y. Chu, S. Zorn, F. Zhang, F. Götz, F. Schreiber, *Int. J. Med. Microbiol.* **2014**, *304*, 949; b) M. Ribeiro, F. J. Monteiro, M. P. Ferraz, *Biomed. Mater.* **2012**, *7*, 045010.
[42] A. G. Gristina, *Science* **1987**, *237*, 1588.
[43] L. Chu, Y. Yang, S. Yang, Q. Fan, Z. Yu, X.-L. Hu, T. D. James, X.-P. He, T. Tang, *Front. Microbiol.* **2018**, *9*, 1.
[44] G. Subbiahdoss, R. Kuijer, D. W. Grijpma, H. C. van der Mei, H. J. Busscher, *Acta Biomater.* **2009**, *5*, 1399.
[45] a) D. Hirayama, T. Iida, H. Nakase, *Int. J. Mol. Sci.* **2017**, 92, *19*; b) C. Leseigneur, P. Lê-Bury, J. Pizarro-Cerdá, O. Dussurget, *Front. Cell. Infect. Microbiol.* **2020**, 10.
[46] a) P. Krzyszczyk, R. Schloss, A. Palmer, F. Berthiaume, *Front. Physiol.* **2018**, 9; b) J. Anderson, S. Cramer, in *Host Response to Biomaterials* (Ed: S. F. Badylak), Academic Press, Oxford **2015**, Ch. 2, p. 13.
[47] a) M. Gatti, S. Barnini, F. Guarracino, E. M. Parisio, M. Spinicci, B. Viaggi, S. D'Arienzo, S. Forni, A. Galano, F. Gemmi, *Antibiotics* **2022**, *11*, 406; b) M. Ribeiro, F. J. Monteiro, M. P. Ferraz, *Biomatter* **2012**, *2*, 176.
[48] C. Atri, F. Z. Guerfali, D. Laouini, *Int. J. Mol. Sci.* **2018**, *19*, 1801.
[49] a) J. D. Thiriot, Y. B. Martinez-Martinez, J. J. Endsley, A. G. Torres, *Pathogens and disease* **2020**, *78*, ftaa009; b) Y. Yao, X.-H. Xu, L. Jin, *Front. Immunol.* **2019**, *10*, 1; c) P. Bortolotti, E. Faure, E. Kipnis, *Front. Immunol.* **2018**, *9*, 1.
[50] S. Ohya, Y. Tanabe, M. Makino, T. Nomura, H. Xiong, M. Arakawa, M. Mitsuyama, *Infect. Immun.* **1998**, *66*, 4043.
[51] a) C. T. Kuo, L. L. Chiang, C. N. Lee, M. C. Yu, K. J. Bai, H. M. Lee, W. S. Lee, J. R. Sheu, C. H. Lin, *J. Biomed. Sci.* **2003**, *10*, 136; b) E. M. Palmieri, C. McGinity, D. A. Wink, D. W. McVicar, *Metabolites* **2020**, *10*, 429.
[52] F. Sjövall, S. Morota, E. Asander Frostner, M. J. Hansson, E. Elmér, *PLoS One* **2014**, *9*, e97673.
[53] S. Chen, A. F. U. H. Saeed, Q. Liu, Q. Jiang, H. Xu, G. G. Xiao, L. Rao, Y. Duo, *Signal Transduct. Target. Ther.* **2023**, *8*, 207.
[54] a) E. M. Palmieri, M. Gonzalez-Cotto, W. A. Baseler, L. C. Davies, B. Ghesquière, N. Maio, C. M. Rice, T. A. Rouault, T. Cassel, R. M. Higashi, A. N. Lane, T. W. M. Fan, D. A. Wink, D. W. McVicar, *Nat. Commun.* **2020**, *11*, 698; b) P. Tripathi, P. Tripathi, L. Kashyap, V. Singh, *FEMS Immunol. Med. Microbiol.* **2007**, *51*, 443; c) H. Jamaati, E. Mortaz, Z. Pajouhi, G. Folkerts, M. Movassaghi, M. Moloudizargari, I. M. Adcock, J. Garssen, *Front. Microbiol.* **2017**, *8*, 1.
[55] S. Pérez, S. Rius-Pérez, *Antioxidants* **2022**, *11*, 1394.
[56] a) M. C. Nielsen, R. Hvidbjerg Gantzel, J. Clària, J. Trebicka, H. J. Møller, H. Grønbæk, *Cells* **2020**, *9*; b) H. A. Valdez, J. L. Marin Franco, J. P. Gorgojo, J. Alvarez Hayes, L. Balboa, M. Fernandez Lahore, M. C. Sasiain, M. E. Rodriguez, *J. Leukocyte Biol.* **2022**, *112*, 173; c) F. Hu, N. Lou, J. Jiao, F. Guo, H. Xiang, D. Shang, *Biomed. Pharmacother.* **2020**, *131*, 110693.
[57] G. J. Kotwal, S. Chien, *Results Probl. Cell Differ.* **2017**, *62*, 353.
[58] a) C. M. Bhadra, M. Werner, V. A. Baulin, V. K. Truong, M. A. Kobaisi, S. H. Nguyen, A. Balcytis, S. Juodkazis, J. Y. Wang, D. E. Mainwaring, R. J. Crawford, E. P. Ivanova, *Nanomicro. Lett.* **2018**, *10*, 1; b) S. Zhao, Z. Li, D. P. Linklater, L. Han, P. Jin, L. Wen, C. Chen, D. Xing, N. Ren, K. Sun, S. Juodkazis, E. P. Ivanova, L. Jiang, *Nano Lett.* **2022**, *22*, 1129.
[59] a) X. Shi, K. Tsuru, L. Xu, G. Kawachi, K. Ishikawa, *Appl. Surf. Sci.* **2013**, *270*, 445; b) J. Barberi, S. Spriano, *Materials* **2021**, *14*, 1590.
[60] a) P. Roach, D. Farrar, C. C. Perry, *J. Am. Chem. Soc.* **2005**, *127*, 8168; b) K. Wang, C. Zhou, Y. Hong, X. Zhang, *Interface Focus* **2012**, *2*, 259.
[61] P. Kallas, H. Valen, M. Hulander, N. Gadegaard, J. Stormonth-Darling, P. O'Reilly, B. Thiede, M. Andersson, H. J. Haugen, *Nanoscale* **2022**, *14*, 7736.
[62] V. Vadillo-Rodríguez, M. A. Pacha-Olivenza, M. L. Gónzalez-Martín, J. M. Bruque, A. M. Gallardo-Moreno, *J. Biomed. Mater. Res., Part A* **2013**, *101A*, 1397.
[63] L. Liang, Q. Huang, H. Wu, H. He, G. Lei, D. Zhao, K. Zhou, *J. Mater. Sci. Technol.* **2022**, *96*, 167.
[64] L. Chen, D. Wang, F. Peng, J. Qiu, L. Ouyang, Y. Qiao, X. Liu, *Nano Lett.* **2019**, *19*, 3480.
[65] B. Wu, Y. Tang, K. Wang, X. Zhou, L. Xiang, *Int. J. Nanomed.* **2022**, *17*, 1865.
[66] R. Bright, D. Fernandes, J. Wood, D. Palms, A. Burzava, N. Ninan, T. Brown, D. Barker, K. Vasilev, *Mater. Today Bio.* **2022**, *13*, 100176.
[67] a) R. M. Visalakshan, M. N. MacGregor, S. Sasidharan, A. Ghazaryan, A. M. Mierczynska-Vasilev, S. Morsbach, V. Mailänder, K. Landfester, J. D. Hayball, K. Vasilev, *ACS Appl. Mater. Interfaces* **2019**, *11*, 27615; b) C. J. Parker, R. N. Frame, M. R. Elstad, *Blood* **1988**, *71*, 86.
[68] R. Bright, A. Hayles, J. Wood, D. Palms, D. Barker, K. Vasilev, *ACS Appl. Bio Mater.* **2023**, *6*, 3472.
[69] S. Franz, S. Rammelt, D. Scharnweber, J. C. Simon, *Biomaterials* **2011**, *32*, 6692.
[70] K. Ishihara, N. P. Ziats, B. P. Tierney, N. Nakabayashi, J. M. Anderson, *J Biomed Mater Res* **1991**, *25*, 1397.
[71] a) Y. Zhu, H. Liang, X. Liu, J. Wu, C. Yang, T. M. Wong, K. Y. H. Kwan, K. M. C. Cheung, S. Wu, K. W. K. Yeung, *Sci. Adv.* **2021**, *7*, eabf6654; b) K. Li, L. Lv, D. Shao, Y. Xie, Y. Cao, X. Zheng, *J. Funct. Biomater.* **2022**, *13*, 31.